1 **The proteasome regulator PSME4 drives immune evasion and abrogates anti-tumor**

2 **immunity in NSCLC**

3

4 Aaron Javitt*[1], Merav D. Shmueli*[1], Matthias P Kramer[1], Aleksandra A. Kolodziejczyk[1], Ivan J.
5 Cohen[1], Iris Kamer[2], Kevin Litchfield[3], Elizabeta Bab-Dinitz[2], Oranit Zadok[2], Vanessa Neiens[4],
6 Adi Ulman[1], Lihi Radomir[1], Hila Wolf-Levy[1], Avital Eisenberg-Lerner[1], Assaf Kacen[1], Michal
7 Alon[5], Ana Toste Rêgo[6], Elvira Stacher-Priehse[7], Michael Lindner[7], Ina Koch[7], Jair Bar[2], Charles
8 Swanton[3], Yardena Samuels[5], Yishai Levin[8], Paula C. A. da Fonseca[6,9], Eran Elinav[1,10], Nir
9 Friedman[1], Silke Meiners[4,11], Yifat Merbl[$][1]
10 *Equal contribution

11
12 [$] Corresponding author: Yifat.merbl@weizmnan.ac.il

13

14   1. Department of Immunology, Weizmann Institute of Science, Rehovot, Israel.
15   2. Institute of Oncology, Sheba Medical Center, and, Faculty of Medicine, Tel Aviv
16   University
17   3. UCL Cancer Institute, CRUK Lung Cancer Centre of Excellence, Cancer Evolution and
18   Genome Instability Laboratory, The Francis Crick Institute, London
19   4. Comprehensive Pneumology Center (CPC), University Hospital, Ludwig-Maximilians
20   University, Helmholtz Zentrum Muenchen, Munich, Member of the German Center for
21   Lung Research (DZL), Germany
22   5. Department of Molecular and Cell Biology, Weizmann Institute of Science, Rehovot,
23   Israel.
24   6. MRC Laboratory of Molecular Biology, Cambridge CB2 0QH, UK.
25   7. Asklepios Lung Clinic Munich-Gauting, 82131, Gauting, Germany.
26   8. de Botton Institute for Protein Profiling, The Nancy and Stephen Grand Israel National
27   Center for Personalized Medicine, Weizmann Institute of Science, Israel.
28   9. Current address: Institute of Molecular Cell & Systems Biology, University of Glasgow
29   10. Division of Cancer-Microbiome Research, DKFZ, Heidelberg, Germany
30   11. Research Center Borstel, Borstel, Germany; Airway Research Center North (ARCN),
31   German Center for Lung Research (DZL), Borstel, Germany.
32   Institute of Experimental Medicine, Christian-Albrechts University Kiel, Kiel, Germany.

33

34

35

36

37 **Graphical Abstract**
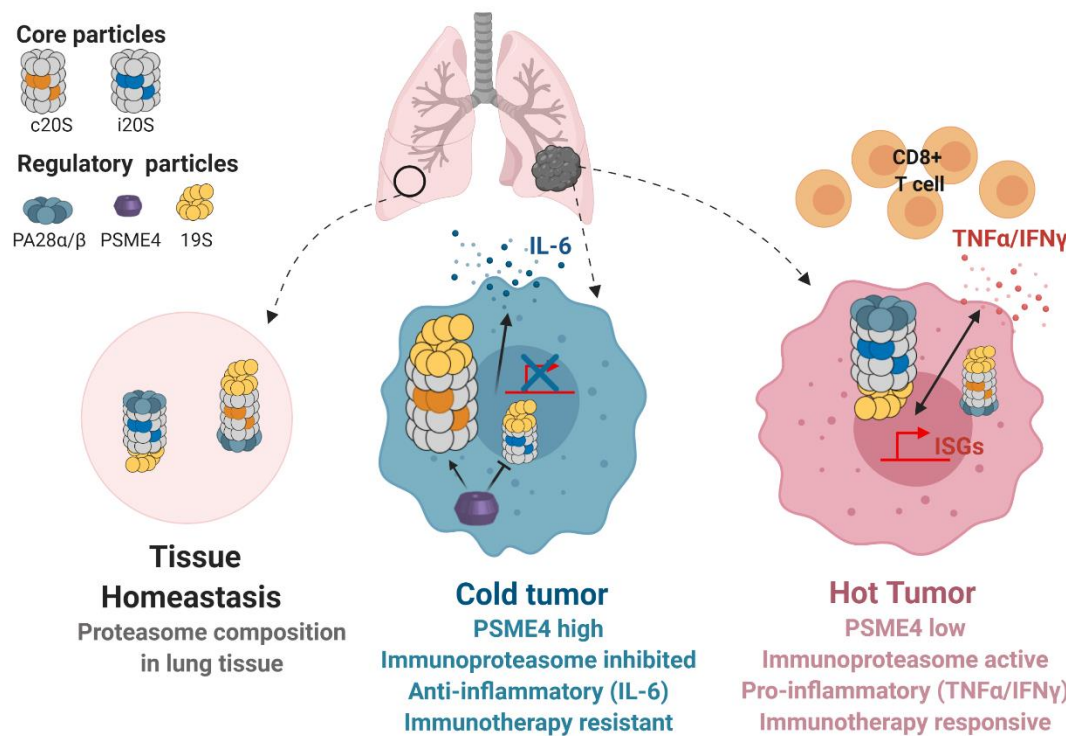
38

39 **Highlights**

40 • Mapping the degradation landscape in Non-Small Cell Lung Cancer (NSCLC) uncovers
41 altered proteasome activity and composition
42 • Proteasome regulator PSME4 plays an anti-inflammatory role in NSCLC by attenuating
43 immunoproteasome activity
44 • PSME4 restricts tumor antigen presentation and cytokine secretion, defining a 'cold' tumor
45 environment
46 • PSME4 drives tumor immune evasion and is associated with resistance to immunotherapy

47 **Summary**

48 Protein degradation by proteasomes is important for the immune response against tumors. Antigens
49 generated by the proteasome promote immune cell infiltration into tumors and improve tumors'
50 responses to immunotherapy. For example, immunoproteasomes – a subset of proteasomes induced
51 by inflammatory signals – may improve the response of melanomas to immune checkpoint
52 inhibitors (ICI) by eliciting tumor inflammation. Yet, it is unclear whether and how protein
53 degradation by proteasomes impacts cancer progression and contributes to immune evasion and
54 resistance. Here, we profile the proteasome-cleaved peptides in lung cancers and find that PSME4
55 serves as a novel inhibitory regulator of the immunoproteasome, playing an anti-inflammatory role
56 in cancer. Biochemical assays combined with scRNA-seq, immunopeptidomics and in vivo
57 analyses demonstrate that PSME4 promotes an immunosuppressive environment around the tumor
58 and abrogates anti-tumor immunity by inhibiting antigen presentation and attenuating tumor
59 inflammation. Furthermore, we find that PSME4 expression is correlated with responsiveness to
60 ICI across several cancer types. Our findings suggest that PSME4-mediated regulation of
61 proteasome activity is a novel mechanism of immune evasion in non-small-cell lung carcinoma and
62 may be targeted therapeutically for restoring anti-tumor immunity.

63
64

65   **Introduction**

66

67   Proteasomal degradation of proteins plays a key role in inflammation and antigen presentation.
68   Further, immunoproteasome upregulation has been associated with response to immune checkpoint
69   inhibitors (ICI; (Ayers et al., 2017; Harel et al., 2019; Kalaora et al., 2020; Riaz et al., 2017a;
70   Rousseau and Bertolotti, 2018; Spits and Neefjes, 2016; Tripathi et al., 2016)), yet whether and
71   how proteasomes may play a role in resistance to therapy remains poorly understood. Tumor
72   immunogenicity is promoted by the switch from constitutive proteasomes to immunoproteasomes
73   that are induced by inflammatory signals (Driscoll et al., 1993; Gaczynska et al., 1993; Salzmann
74   et al., 1999; Winter et al., 2017). The canonical constitutive- and immunoproteasomes differ by
75   three catalytic subunits Psmb8, Psmb9 and Psmb10 that are encoding the proteins LMP7, LMP2
76   and MECL1, respectively. The immunoproteasome is induced by inflammatory cytokines (e.g.
77   IFN) and is basally expressed mainly in immune cells (Driscoll et al., 1993; Gaczynska et al., 1993;
78   Salzmann et al., 1999). Previous studies uncovered an altered cleavage pattern by the
79   immunoproteasome, which is responsible for generating more hydrophobic peptides, that are
80   thought to be preferential for binding the Transporter associated with antigen processing (TAP) and
81   MHC class I presentation (Chong et al., 2018; Javitt et al., 2019a; Rock et al., 2016). Beyond
82   antigenicity, immunoproteasomes have also been suggested to increase cellular inflammation by
83   attenuating IL-6 secretion and promoting inflammatory cytokine secretion (Arima et al., 2011;
84   Ferrington and Gregerson, 2012; Kammerl and Meiners, 2016; Kitamura et al., 2011; Liu et al.,
85   2012; Muchamuel et al., 2009; Schmidt et al., 2018). However, whether and how tumorigenic
86   mechanisms modulate the immunoproteasome and constitutive proteasome functions to shape their
87   microenvironments remains poorly understood.

88

89   In addition to the core particle of the proteasome ,proteasome composition and the degradation
90   landscape may be affected by specific regulatory particles such as the 19S regulatory complex
91   (PSMC1-6 and PSMD1-14), or the regulatory caps PA28αβ (PSME1-2), PA28γ (PSME3) or
92   PA200 (PSME4) (Collins and Goldberg, 2017; Coux et al., 2020; Rousseau and Bertolotti, 2018)
93   that bind the catalytic core and affect gate opening and substrate selection. The 19S regulatory
94   complex been shown to be pivotal for binding of ubiquitinated species and substrate unfolding,
95   while the other regulatory subunits are suggested to have more specialized roles, including
96   mediating inflammatory responses, histone degradation, and the response to DNA damage
97   (Antoniou et al., 2012; Blickwedehl et al., 2012; Collins and Goldberg, 2017; Khor et al., 2006;
98   Mandemaker et al., 2018a, 2018b; Qian et al., 2013; Rousseau and Bertolotti, 2018; Ustrell et al.,
99   2002; Welk et al., 2016). The different catalytic cores, together with the diverse range of regulatory
100   subunits, introduce great potential diversity for generating hybrid proteasomes of the 20S core
101   particle with different combinations of regulatory caps, thereby altering protein cleavage (Fabre et
102   al., 2014, 2015; Morozov and Karpov, 2019; Raule et al., 2014; Toste Rêgo and da Fonseca, 2019).
103   However, it remains underexplored how the regulatory and catalytic subunits shape tumor-host
104   interactions.

105

106   Here, we analyzed, for the first time the degradation landscape in clinical samples of resected
107   tumors and found a distinct signature that was associated with NSCLC. Altered proteasome activity
108   in the cancerous tissue revealed an altered composition of proteasomes, with significant
109   upregulation of the regulatory cap, PSME4, which was associated with poor survival. Exacting
110   functional and biochemical assays together with single cell RNA analysis and in vivo work
111   surprisingly revealed that, PSME4-capped immunoproteasomes, which were not described before,
112   directly attenuate the catalytic activity of the immunoproteasome. We could further show that
113   PSME4-capped constitutive proteasomes exhibited an increase in caspase-like activity in NSCLC.
114   These marked opposing effects upon binding of PSME4 to the constitutive or immuno-
115   proteasomes, in turn, lead to decreased tumor immunogenicity and contribute to tumor growth *in*

116 *vivo*. Further, we show that PSME4-associated proteasomes play an anti-inflammatory role in
117 NSCLC, and that PSME4 promotes a 'cold' tumor signature associated with resistance to ICI across
118 cancer types. Collectively, our findings uncover new insight into the degradation landscape of
119 NSCLC and elucidate a causal role of PSME4 in shaping the tumor microenvironment to suppress
120 anti-tumor immunity. Together, our work introduces a novel paradigm by which proteasome
121 composition and heterogeneity should be examined in the context of cancer and response to
122 immunotherapy in NSCLC and beyond.
123
124 **Results**
125
126 **Proteasome profiling reveals an altered proteasome activity and distinct cleavage patterns in**
127 **lung adenocarcinoma**
128 To address these questions, we utilized our recently established proteasome profiling approach for
129 Mass spectrometry analysis of proteolytic peptides(Javitt and Merbl, 2019; Wolf-Levy et al., 2018)
130 (MAPP) to analyze tissue samples of non-small cell lung cancer (NSCLC) and adjacent tissue
131 controls from the same lungs, processed in parallel. We then isolated proteasomes from tumor
132 samples and analyzed the nascent peptides that were either 'trapped' inside or closely associated
133 with the proteasomes to detect patterns of degradation in single peptide resolution (Figure 1A).
134 Proteomic analysis of both protein abundance and degradation revealed that different tumors had
135 shared patterns of degradation that were distinguished from those of the adjacent control tissues
136 (Figures S1A-D). Detailed examination of the substrates highlighted cellular targets that were
137 readily detected in tumor tissues, some of which (e.g. CASC5; Figures 1B) are associated with
138 cancer and are not expected to be expressed in the healthy lung. Notably, some of the degradation
139 targets were not detected at all by the proteomic analysis, suggesting that they might be rapidly
140 degraded and therefore not accumulating in cells to reach a level that is detectable by mass
141 spectrometry analysis (Figures 1C, S2A-B).
142
143 Beyond specific degradation substrates, we found an increase in nuclear proteins that were
144 degraded in the cancerous tissues (Figures S3A-C). Further, we found significant alterations in the
145 cleavage pattern of substrates in the cancerous tissue (Figure 1D). Specifically, the carboxy
146 terminal residue of the degraded peptides, which is the site of proteasome cleavage, differed
147 between the tumor and adjacent samples (Figures. 1D). These observations suggested that
148 proteasome composition and function may be altered in NSCLC. We therefore examined the
149 protein abundance of different proteasome subunits. Proteasome complexes are comprised of the
150 core particle, which process the substrates, and regulatory caps, which control substrate
151 entry(Collins and Goldberg, 2017; Coux et al., 2020; Livneh et al., 2016; Motosugi and Murata,
152 2019; Rodriguez et al., 2007; Rousseau and Bertolotti, 2018). Notably, while subunits of the
153 proteasome core particle (e.g. 20S and i20S) were similar between the tumor and adjacent tissues,
154 the regulatory cap PSME4 (also known as PA200) was significantly upregulated in the cancerous
155 tissue (Figures 1E-F). We confirmed that PSME4 is upregulated in the cancerous tissue using
156 CPTAC proteomics (Gillette et al., 2020) and 2 additional patient cohorts (Figures 1G-H, S4A-C).
157 As previously reported (Khor et al., 2006) we found PSME4 was localized mainly to the nucleus
158 (Figure 1I, S4D-E). Notably, we showed that high PSME4 levels in lung cancer were associated
159 with poor prognosis of NSCLC patients (Mantel-Cox p value = 0.038, Figures 1J and S5A).
160 However, we did not observe any association in this cohort between PSME4 abundance and
161 NSCLC subtype, smoking or tumor stage (Figure S5A-E). Together, these results show that the
162 proteasome composition and proteasome-associated cleavages are changed in NSCLC and
163 suggested that PSME4 may impact tumor growth through modulating proteasome activity.
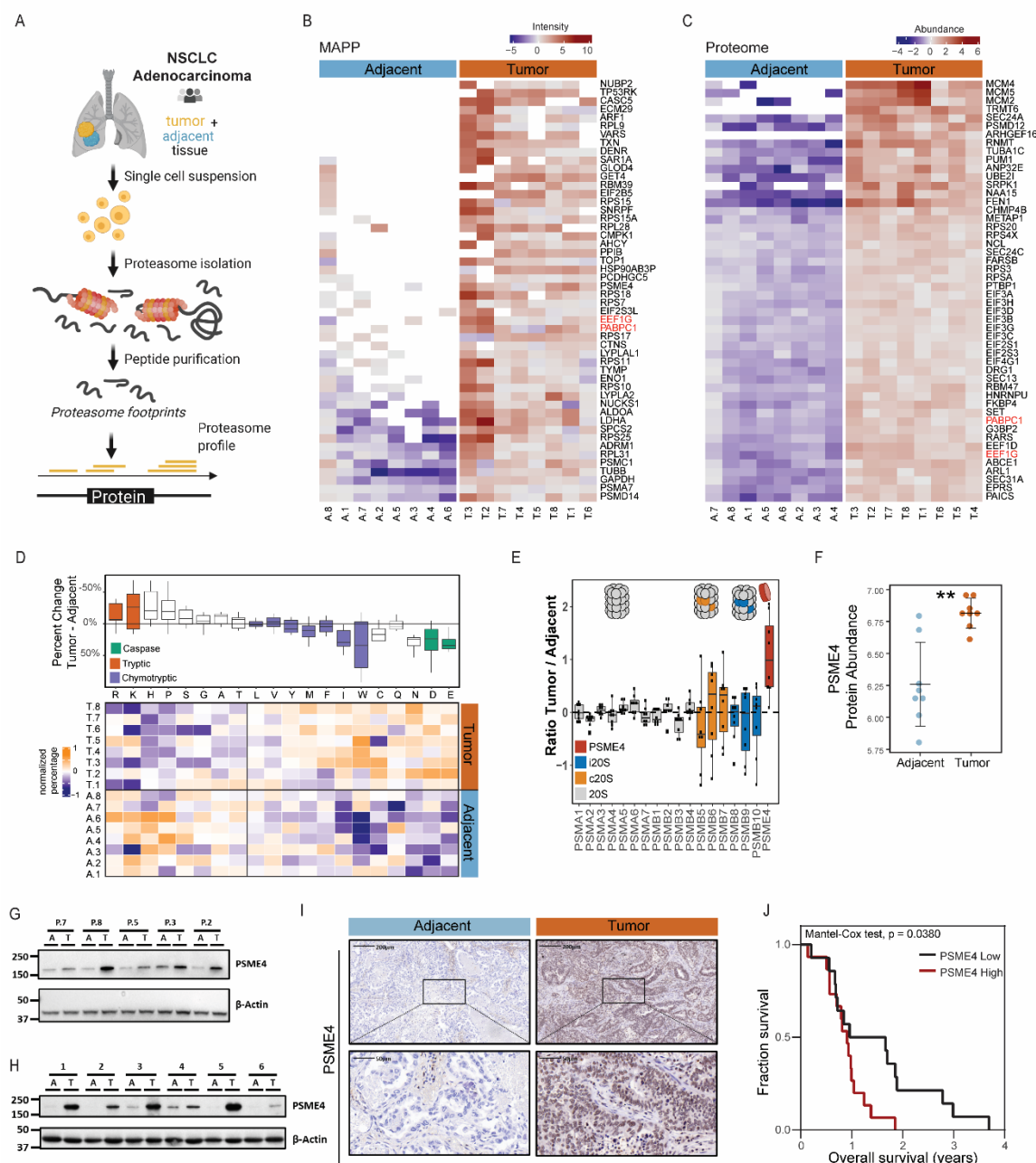
Fig 1. Proteasome profiling reveals an altered proteasome activity and distinct cleavage patterns in lung adenocarcinoma (A) Schematic representation of the workflow. Analysis of lung adenocarcinoma and adjacent lung tissue was performed using standard whole cell extract proteomics to assess protein abundance and MAPP to study the proteasome composition and degradome of the sample (N=8 tumor and 8 adjacent sections). **(B-C)** The top 50 most tumor-associated proteins as identified by MAPP (B) or whole cell Proteomics (C) are shown for each of the tumor and adjacent samples. The proteins in both lists are marked in red. **(D)** MAPP identified peptides were divided based on their carboxy terminal residue. The percentage of peptides with each terminus was calculated for each sample and normalized across patient samples. Amino acids are annotated with their matching proteasome cleavage activity; rows are clustered using Pearson distances. The bars represent the percent change for each amino acid at the carboxy terminus comparing tumors and adjacent tissues. **(E)** The ratio between subunit abundance in the proteasome immunoprecipitated from tumor and adjacent tissue per patient. Colors and diagrams indicate the identity of the proteasome subunits. **(F)** PSME4 abundant in the pulldown from tumor samples and from adjacent tissues (**Wilcoxon

178   P = 0.0078). **(G-H)** Tumor (T) and adjacent (A) tissues from an Israeli (G) or German (H) cohort was
179   immunoblotted for PSME4. β-Actin was used as a loading control. **(I)** Immunohistochemistry of PSME4 in
180   the tumor and adjacent tissues shows increased abundance in the tumor tissue with nuclear localization in
181   both. **(J)** Surviving analysis shows that patients having lung tumors with increased staining of PSME4
182   (immunohistochemistry) had significantly reduced survival compared to patients with lung tumors
183   expressing low levels of PSME4 (Mantel-Cox test p = 0.0380).

184

PSME4 restricts immunoproteasome activity and reduces immunopeptidome diversity and cellular inflammation

187   Proteolytic activities of the constitutive proteasome and immunoproteasome are different(Driscoll
188   et al., 1993; Gaczynska et al., 1993; Salzmann et al., 1999; Winter et al., 2017). We therefore
189   assessed whether the PSME4 level was associated with the function of both proteasome subtypes
190   in patient-derived tumor samples. Notably, the caspase- and chymotryptic-like cleavage activities
191   of the proteasome positively correlated, whereas tryptic-like cleavage negatively correlated with
192   the abundance of PSME4 (Figures 2A-B, S6A). This could not be explained by a general shift in
193   the amino acid composition across the degraded substrates (Figure 2C). PSME4 has been
194   previously shown to alter cleavage specificity of the constitutive proteasome(Blickwedehl et al.,
195   2012; Toste Rêgo and da Fonseca, 2019; Ustrell et al., 2002). However, it was not known if and
196   how PSME4 affected the activity of the immunoproteasome (Figure 2D). We found by biochemical
197   examination that PSME4 bound both constitutive proteasome and immunoproteasome in a human
198   lung cancer cell line (Figure 2E, S6B-D), suggesting that PSME4 can affect the activity of the two
199   proteasome subpopulations independently. We then assessed the effect of supplementing
200   recombinant PSME4 on the proteasome activity in vitro using model substrates for defined
201   constitutive cleavage sites. This system allowed us to decouple the effect of PSME4 on the
202   proteasome from potential transcriptional effects that have been reported in other
203   settings(Blickwedehl et al., 2012; Qian et al., 2013). We found that the caspase-like (β1) activity
204   increased (Figure 2F, S7A-D) whereas the tryptic-like (β2) activity decreased upon PSME4
205   supplementation (Figure 2G and S7E), corroborating our above results from clinical samples
206   (Figures 2A-B). Surprisingly, PSME4 had opposite effects on the constitutive proteasome β1 and
207   its immunoproteasome counterpart β1i subunit, increasing the former and inhibiting the latter
208   (Figures 2H, S7F). In fact, PSME4 inhibited all immunoproteasome-associated activities (β1i, β2i
209   and β5i) under inflammatory stimulation (Figures S7F-H), in which the immunoproteasome is
210   predominant. Thus, PSME4 is the first proteasomal subunit identified that inhibits the
211   immunoproteasome activity.

212

213   Proteasome-cleaved peptides serve as the major source of antigens presented by class I MHC. Both
214   the observed PSME4-mediated increase in caspase-like activity and decrease in tryptic-like activity
215   suggested generating peptides that are less favorable for MHC-I presentation. We therefore
216   hypothesized that PSME4 might counteract the generation of antigenic epitopes by the
217   immunoproteasome and decrease tumor antigenicity. To address this question, we performed HLA
218   immunopeptidomics of lung cancer cells with and without overexpressing PSME4 (Figure S8A).
219   We identified 463 peptides (10% of the identified peptides) that were significantly changed upon
220   PSME4 overexpression compared to the control (Figure S8B). As caspase-cleaved peptides do not
221   bind well to the MHC (Javitt et al., 2019a; O'Donnell et al., 2020), they are not highly presented
222   in either condition. Yet, the percentage of peptides with tryptic termini were decreased following
223   PSME4 overexpression (Figure 2I), corresponding to the PSME4-driven change in proteasome
224   activity (Figure 2B). Further, examination of the protein source of the presented peptides, we found
225   an enrichment of nuclear proteins in the immunopeptidome following PSME4 overexpression
226   (Figure S8C). Finally, when examining the distribution of amino acids across the differentially
227   presented peptides, we found that the peptides presented in the PSME4-overexpresing cells were

228   less diverse than those in the control (Figures 2J-K). Notably, only 4 residues in the overexpressing
229   cells, compared to 9 residues in the control, make up 80% of the carboxy-termini of the peptides
230   associated with MHC binding, indicating that PSME4 overexpression significantly restricts the
231   diversity of presented antigens (Figures 2J-K). As PSME4 was previously reported to be
232   incorporated in only a small percentage of proteasome complexes (Fabre et al., 2014; Morozov and
233   Karpov, 2019) we sought to examine whether depleting it would impact significantly the
234   immunopeptidome. In accordance, we could show that depleting PSME4 (Figures S9A-C)
235   significantly increased antigen presentation, as exhibited by 30% increase in surface HLA
236   molecules (Figures 2L and S10). Together these results suggest that PSME4 decreases the diversity
237   of the cellular immunopeptidome, attenuates antigen presentation and immunoproteasome activity.
238
239   **PSME4 reduces cellular inflammation and cytokine secretion**
240   Beyond antigenicity, the immunoproteasome has been previously implicated in modulating
241   inflammation by modulating cytokine secretion(Arima et al., 2011; Ferrington and Gregerson,
242   2012; Kammerl and Meiners, 2016; Kitamura et al., 2011; Liu et al., 2012; Muchamuel et al., 2009;
243   Schmidt et al., 2018). We therefore hypothesized that PSME4 might promote an
244   immunosuppressive environment by direct prohibiting tumor inflammation, in addition to
245   modulating antigenicity. To gain insight into the functional consequences of upregulation of
246   PSME4 in NSCLC, we stratified patient tumors from The Cancer Genome Atlas (TCGA) based on
247   their PSME4 expression levels and associated them with cellular functions (Figure S11A). We
248   found that PSME4-high tumors were enriched with pathways related to cell cycle and DNA
249   replication (Figure S11B), whereas PSME4-low tumors were associated with a number of immune
250   and inflammation-related pathways (Figure 3A). To examine whether there might be a causal
251   relationship between PSME4 and cancer inflammation, Proteomic analysis revealed that IFN
252   signaling pathways were enriched in the PSME4-depleted cells following inflammatory stimulation
253   (Figure 3B, S11C-D).
254
255   Furthermore, we found increased abundance of multiple components of the antigen presentation
256   machinery (e.g. TAP1; Figure 3B) in the PSME4 depleted cells in accordance with the observed
257   increase in surface HLA (Figure 2L). By contrast, KRAS signaling and epithelial to mesenchymal
258   transition (EMT) pathways, which have been previously associated with immunoproteasome-
259   deficient lung cancer (Tripathi et al., 2016) were also enriched here in control conditions with high
260   PSME4 (Figure S11D). Likewise, we found that depleting PSME4 significantly increased the
261   expression of IFN-inducible genes, such as IFIT1 and ISG15 (Figure 3C, S11E-F). Interestingly,
262   STAT1 and STAT2 were more abundant whereas STAT3 and STAT5 were reduced in PSME4-
263   depleted cells than in control cells (Figures 3D). STAT1 and STAT3 have previously been shown
264   to play opposing roles in cancer-related inflammation with STAT3 serving a pro-oncogenic
265   role(Avalle et al., 2012). Consistent with this, we also observed decreased IL6 expression upon
266   PSME4 depletion in two lung cancer cell lines (Figures. 3E, S11D-E). IL-6 is a hallmark of STAT3
267   signaling and serves an anti-inflammatory and pro-oncogenic role in tumor cells(Avalle et al., 2012;
268   Johnson et al., 2018). Thus, we hypothesized that the upregulation of PSME4 in lung cancer may
269   directly attenuate tumor inflammation and drive immune suppression in the microenvironment by
270   modulating IL-6 expression.
271
272   To determine the effect of PSME4 on cytokine secretion in the tumor microenvironment, we
273   utilized the KP1.9 cells derived from a $Kras^{G12D};Trp53^{-/-}$ murine lung adenocarcinoma in an
274   orthotopic murine model. We established KP1.9 isogenic cell lines with either ectopic expression
275   (KP1.9$^{PSME4\_OE}$) or knockdown (KP1.9$^{PSME4\_KD}$) of PSME4 (Figures S12A-F). Depletion of PSME4
276   reduced its levels to be comparable with those of normal lung epithelial cells (Figure S12C). We
277   first examined the cytokine profile of these cell lines and found that TNFα, IFNγ and IL-17a were
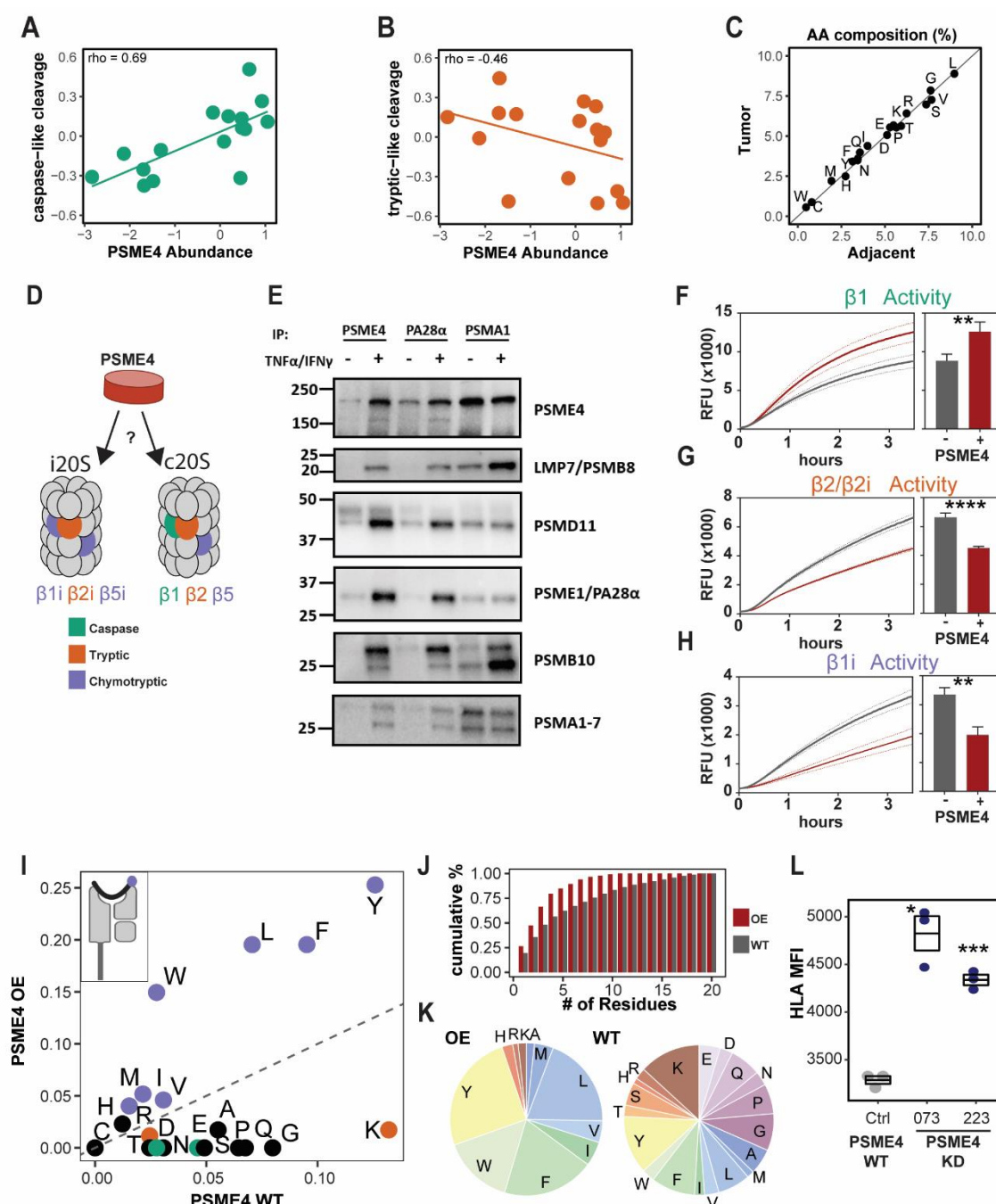
278
279 **Fig 2. PSME4 restricts proteasome activities and reduces immunopeptidome diversity**. (**A – B**) The
280 carboxy terminal residue of peptides was used to classify peptides based on the proteasome activity attributed
281 to their cleavage. The abundance of PSME4 in the samples based on WC proteomics correlated with the
282 caspase-like signature (A; spearman rho = 0.69) and was anti-correlated with the tryptic-like signature (B;
283 spearman rho = -0.46). (**C**) The average amino acid percent composition for all the peptides identified by MAPP
284 in the tumor samples (y-axis) is plotted against the corresponding adjacent samples. (x-axis). (**D**) Schematic
285 representation of the constitutive proteasome (c20S) and immunoproteasome (i20S) with associated catalytic
286 subunits. (**E**) Proteasome complexes were immunoprecipitated (IP) with the indicated antibody from A549
287 cells that were either treated with TNFα and IFNγ or left untreated and blotted for the indicated proteasome
288 subunits. (**F-H**) Proteasome activity assays using the nLPnLD-AMC (F), RLR-AMC (G) or PAL-AMC (H)
289 fluorogenic substrate to measure the activity of indicated subunits. Relative fluorescence (RFU) of the substrate

290 is shown across the 3.5 hours of the experiment (left) or at the endpoint (right). A549 lysates were untreated
291 (F), to measure the constitutive proteasome activity, or treated with TNFα and IFNγ (G and H), to measure the
292 immunoproteasome activity. Recombinant PSME4 was added to the lysate where indicated (red, paired T-test;
293 **P <0.01, **** P < 0.0001). (**I**) The percentage of each amino acid in the carboxy terminus of the peptides
294 differentially presented on MHC molecules in the A549 cells overexpressing PSME4 (PSME4 OE) vs. empty
295 vector control (PSME4 WT) are shown in a scatter plot. Residues are colored based on the associated cleavage
296 activity: green - caspase, purple – chymotryptic and orange – tryptic; and a dotted line is shown for X=Y. (**J**)
297 The cumulative percentage of peptides explained by the number of different amino acids (from one to all twenty)
298 at the carboxy terminus (end position) in PSME4 WT (WT, grey) and PSME4 OE (OE, red) immunopeptidome.
299 (**K**) The percentage of each amino acid in the carboxy terminus of the peptides differentially presented on MHC
300 molecules in the A549 cells overexpressing PSME4 (PSME4 OE) vs. empty vector control (PSME4 WT). (**L**)
301 Median fluorescence intensity from flow cytometry analysis of MHC-I expression using a pan HLA-A/B/C
302 antibody (W6/32) for A549 cells with PSME4 knockdown (shA223 and shA073) or control (shCtrl). The HLA
303 mean fluorescent intensity (MFI) is significantly higher in the PSME4 knockdown compared to the control (*
304 P = 0.01, *** P = 0.0001).

306 Increased while IL-6 and MIP-1α were decreased by the depletion of PSME4 (Figure 3F),
307 consistent with the observed changes in the human lung cancer cell line. Importantly, the
308 immunoproteasome has been previously implicated in modulating cytokine secretion, primarily in
309 the context of lymphocytes(Arima et al., 2011; Kitamura et al., 2011; Liu et al., 2012; Muchamuel
310 et al., 2009; Schmidt et al., 2018). For example, mutations in immunoproteasome subunits that limit
311 the proteasomal activity increase IL-6 secretion(Arima et al., 2011). We therefore hypothesized
312 that PSME4-mediated restriction of immunoproteasome activity in cancer cells might directly
313 increase tumor IL-6 secretion. Indeed, blocking immunoproteasome activity with ONX0914
314 partially rescued the loss of IL6 secretion from PSME4-depleted KP1.9 cells, suggesting that
315 modulation of immunoproteasome activity contributes to the effect of PSME4 on IL-6 expression
316 (Figures 3G, S12G-I). Furthermore, inhibiting the immunoproteasome almost completely
317 abrogated the increase in IL-17 secretion in PSME4-depleted cells (Figures 3H).

319 **PSME4 promotes an immunosuppressive tumor microenvironment**
320 As tumor inflammation and antigenicity are key to anti-tumor immunity, we examined the effect
321 of PSME4 *in vivo* by injecting mice with KP1.9, KP1.9$^{PSME4\ OE}$ or KP1.9$^{PSME4\_KD}$ (Figures 4A).
322 Notably, mice bearing KP1.9$^{PSME4\ OE}$ showed marked reduction in their body weight starting a
323 month from tumor cell injection (33 days), as compared to mice bearing KP1.9 tumors (Figure
324 S13A). Lungs of mice bearing KP1.9$^{PSME4\ OE}$ tumor were significantly larger, contained numerous
325 lesions whereas lungs of mice bearing KP1.9$^{PSME4\ KD}$ did not show any detectable lesions (Figures
326 4B-C, S13B-D). These effects were not driven by a change in the proliferation rate of tumor cells
327 (Figures S13E-F). Next, we analyzed the changes in the immune milieu by performing single cell
328 RNA sequencing (sc-RNA seq) of CD45+ cells 3 weeks after the injection of parental KP1.9 or
329 KP1.9$^{PSME4\ KD}$ tumor cells. This allowed us to examine the effect of PSME4 on the early immune
330 response to the tumor, without bias due to dramatically different levels of tumor burden (Figures
331 4D-E S14A-B). The overall distribution of cell types was similar among groups (Figure S14A).
332 However, the relative sizes of the alveolar and cycling macrophage clusters as well as *Ccr7+*
333 regulatory DCs, which have been previously shown to play an immunosuppressive role in NSCLC
334 (Lavin et al., 2017; Maier et al., 2020), in the lung of mice bearing KP1.9$^{PSME4\ KD}$ tumors were
335 smaller than in the lung of mice bearing KP1.9 tumors (Figures 4F-H). Interestingly, we
336 concurrently observed a decrease in the secretion of the macrophage recruiting chemokine MIP-
337 1α/CCL3 (Baba and Mukaida, 2014) from the KP1.9 tumor cells upon PSME4 depletion (Figure
338 3F). We also observed an increase in plasmacytoid DCs (pDCs) in the mice bearing KP1.9$^{PSME4\ KD}$
339 tumors (Figure 4I). While pDCs have been proposed to have both pro- and anti-inflammatory roles
340 in cancers(Li et al., 2017), here we see the expression of *Il12a* and an enrichment for pathways
341 related to antigen presentation and processing (Figure 4J, S15A-B), suggesting that pDCs serve a
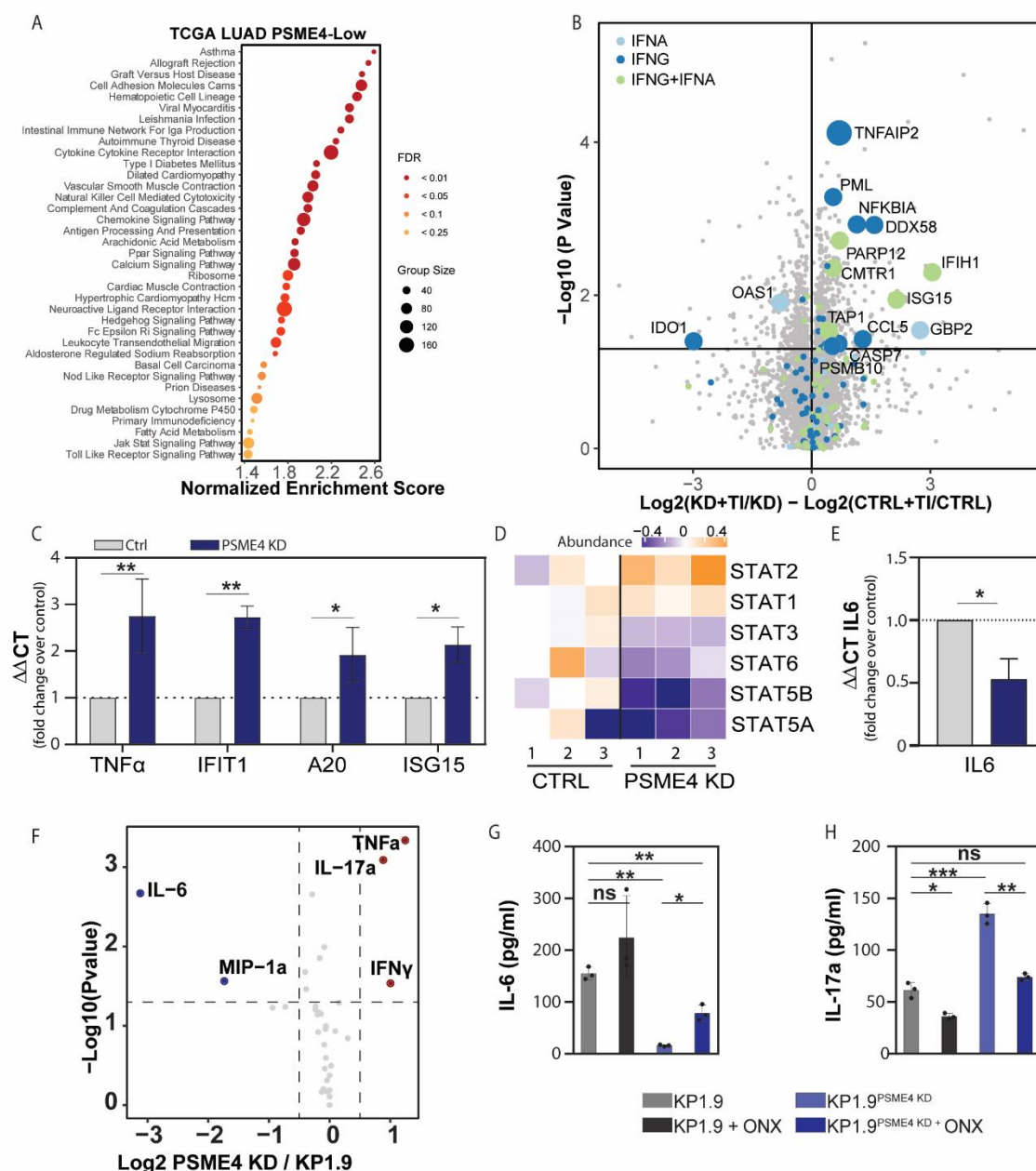
Fig. 3 Depleting PSME4 increases cellular inflammation and cytokine secretion (A) TCGA LUAD samples were stratified by PSME4 expression and PSME4- high samples were compared to PSME4- low (n = 230 samples). The normalized enrichment score for KEGG pathways significantly overrepresented in PSME4-low samples are shown. Dot color indicates FDR threshold and size indicates number of genes in the pathway (Group Size). **(B)** The difference of the log2 transformed ratio of protein abundances following stimulation with TNFα and IFNγ (TI) compared to unstimulated (UT) between PSME4 depleted A549 cells (shPSME4) and control (shCtrl) is plotted against the negative log10 transformed p value for a student's t test comparing the two ratios. Proteins involved in IFN signaling are marked (light blue: response to IFN-alpha (GO: 0035455) dark blue: response to IFN-gamma (GO:0034341), or green: proteins in both lists). Points that significantly differed between the two conditions (student's t test $P \leq 0.05$) and are annotated as IFN signaling pathway components are labeled with the gene name. **(C)** qPCR of genes downstream to IFNγ activation (TNFα, IFIT1, A20 and ISG15) following stimulation with TNFα and IFNγ. A549 cells expressing shPSME4 are compared to those expressing shCtrl (paired T test **$P < 0.01$ and *$P \leq 0.05$). **(D)** Abundance of STAT proteins from shPSME4 -or shCtrl-expressing cells stimulated with TNFα and IFNγ. **(E)** qPCR of IL6 in A549 cells

357 expressing shPSME4 (blue) or shCtrl (grey) following stimulation with TNFα and IFNγ (students' T test *P ≤
358 0.05). **(F)** The log2 transformed ratio of the level of secreted indicated cytokines between PSME4-deficient
359 (KD) and control (KP1.9) KP1.9 cells following stimulation with TNFα and IFNγ is plotted against the negative
360 log10 transformed p value. **(G-H)** The amount of IL-6 (G) or IL-17a (H) secreted from KP1.9 or PSME4-
361 deficient KP1.9 cells following stimulation with TNFα and IFNγ, with or without the immunoproteasome
362 inhibitor ONX-0914 (ONX). Cytokines are measures in pg per ml (student's T test (ns P>0.05, *P<0.05,**P <
363 0.01, ***P < 0.001).

364

365 pro-inflammatory role in this context. This is in contrast to the mature DCs enriched in
366 immunoregulatory molecules (mregDCs), which are decreased in KP1.9$^{PSME4\_KD}$ and express higher
367 levels of *Il6* (Figure 4K, S15C-D). Likewise, the increased secretion of IFNγ upon PSME4
368 depletion was accompanied by an increase in the expression of IFN response gene *Ifi272a* in several
369 cell types, including interstitial macrophages, cycling dendritic cells and Tregs (Figure 4L). Finally,
370 to examine if there is a skew towards particular cell fates, we characterized the T cell populations
371 and T cell receptors (TCR). We reasoned that TCR clones that were not unique were result of
372 expansion (Figures. 4M, S16A-B). We found that cytotoxic T cell and regulatory T cell populations
373 had considerably expanded (Figures S17A-B, S18A-D). There were more cytotoxic CD8 T cells in
374 the KP1.9$^{PSME4\ KD}$ milieu whereas Tregs expanded in the KP1.9 bearing mice, with a significant
375 difference in the Treg/CD8 T cell ratio between the two groups (Figure 4N). Together, our results
376 suggest that upregulation of PSME4 may both drive immune evasion by reducing cytotoxic T cell
377 activity and play an active role in tumorigenesis by promoting an immune-suppressed
378 microenvironment *in vivo*.

379

380 To further validate the changes observed by scRNA-seq, we analyzed the lung of tumor-bearing
381 mice and stained for tumor infiltrating lymphocytes (TILs, Figure 5A, S19A-D). Here too, we
382 found that KP1.9$^{PSME4\ OE}$ tumors exhibited a decrease in the CD8$^+$ T cell/Treg ratio (Figures 5A-B).
383 Moreover, our analysis revealed a significant increase in exhausted PD1$^+$ CD8$^+$ T cells (Figure 5C
384 and S19A) and a decrease in IFNγ in tumor infiltrating lymphocytes (TILs) in KP1.9$^{PSME4\ OE}$ tumor-
385 bearing mice (Figure 5D-E), suggesting decreased tumor inflammation. Furthermore, we observed
386 a decrease in naïve CD8$^+$ T cells (CD62L+, CD44-; Figures 5F-G, S20B-C) suggesting that
387 KP1.9$^{PSME4\ OE}$ exhibit reduced inflammation and T cell activation. To determine whether the
388 PSME4-induced effect on tumor growth was indeed immune-mediated, we repeated the experiment
389 using RAG1-deficient mice, which lack lymphocytes. In contrast to WT mice where the KP1.9-
390 bearing mice lost weight more quickly than the KP1.9$^{PSME4\ KD}$, no differences in weight loss or
391 survival between mice bearing PSME4-deficient and those bearing KP1.9 tumors (Figure S21)
392 were observed, further corroborating that the PSME4-driven changes in tumor progression is
393 mediated by lymphocytes *in vivo*. To further consolidate this point we tested the ability of
394 splenocytes isolated from tumor-bearing mice to kill the tumor cells. We found that splenic
395 lymphocytes from mice bearing KP1.9$^{PSME4\ OE}$ tumors exhibited reduced propensity to kill KP1.9
396 cells (Figures 5H S22A). By contrast, splenic lymphocytes from mice bearing KP1.9$^{PSME4\ KD}$ tumor
397 demonstrated killing even better than those from mice bearing KP1.9 tumors (Figure 5H). These
398 results indicated that the anti-tumor activity we observed indeed depended on loss of PSME4.
399 Accordingly, we found a significant increase in a Th17-associated cytokine signature (IL-22, IL-
400 17a and IFNγ), which is associated with promoting CD8 cell anti-tumor responses(Knochelmann
401 et al., 2018), in the secretome of splenic lymphocytes from mice bearing KP1.9$^{PSME4\ KD}$ tumors
402 (Figures 5I-K, S22B-D). These findings were in agreement with our observation that depletion of
403 PSME4 induces the secretion of IL-6, a key cytokine regulating the Treg / Th17 balance by
404 inhibiting Treg and promoting Th17 differentiation (Kimura and Kishimoto, 2010).
405

406
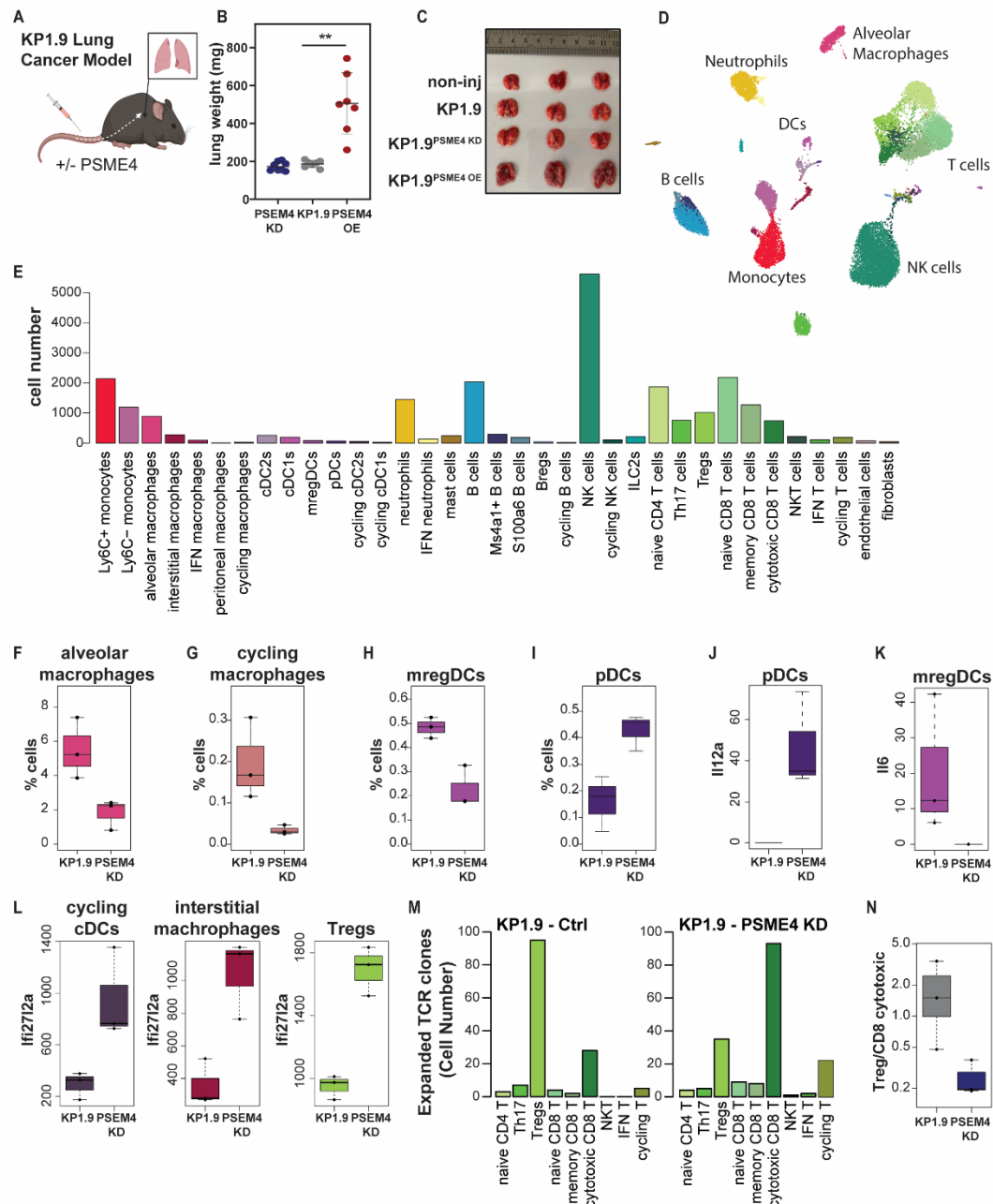
Fig. 4 PSME4 promotes an immunosuppressive tumor environment (A) Schematic of orthotopic lung tumor models by tail vein injection of KP1.9 cells overexpressing (KP1.9$^{PSME4\ OE}$) or deficient of (KP1.9$^{PSME4\ KD}$) PSME4 to C57/B6 mice **(B)** The lung weight of mice bearing parental, PSME4-overexpressing (OE), or PSME4-deficint (KD) KP1.9 tumors (**P = 0.0020). **(C)** Photograph of representative lungs from mice not injected with tumor cells (non-inj) 41 days after the injection of parental, PSME4 overexpressing (OE), or PSME4 deficient (KD) KP1.9 cells. **(D)** Uniform manifold approximation and projection visualization (UMAP) showing 35 cell populations across the three replicates from mice bearing KP1.9 (Ctrl) or KP1.9$^{PSME4\ KD}$ tumors. **(E)** Bar graph showing total number of cells per cell type identified across the three replicates from mice bearing KP1.9 (Ctrl) or KP1.9$^{PSME4\ KD}$ tumors (KD). **(F-I)** Boxplot showing relative abundance of alveolar macrophages (F), cycling macrophages (G), mature DCs enriched in immunoregulatory molecules (mregDCs) (H), and plasmacytoid DCs (pDCs) (I) in the lung of mice injected with KP1.9 (n = 3) or KP1.9$^{PSME4\ KD}$ (PSEM4KD) (n = 3) cells. Boxplot shows 25th to 75th percentiles with the 50th denoted by a line; whiskers show 1.5× interquartile range, or maximum or minimum if smaller. **(J,**

-12-

420 **K)** Boxplot showing pseudobulk tpm expression of *Il6* in mregDCs (J) or expression of *Il12a* in pDCs (K) in
421 the lung of mice injected with KP1.9 (n = 3) or KP1.9^PSME4 KD (PSEM4KD) (n = 3) cells. **(L)** Boxplots
422 showing pseudobulk tpm expression of *Ifi27l2a* in cycling cDCs, interstitial macrophages and regulatory T
423 cells in the lung of mice injected with KP1.9 (n = 3) or KP1.9 PSEM4KD) (n = 3) cells. **(M)** Barplot showing
424 number of TCR clones which were expanded (at least 2 cells sharing the same TCR clone) in the different T
425 cell populations in a representative samples from mice injected with KP1.9 or KP1.9 PSEM4 depleted
426 (PSEM4KD) cells. **(N)** Ratio of number of expanded (i.e. having non-unique TCR) Tregs to cytotoxic CD8
427 ratio in each sample.

428

429 **PSME4 drives a 'cold' tumor signature in NSCLC and is associated with reduced response**
430 **to ICI across multiple cancer types.**
431 Our findings that PSME4 plays an anti-inflammatory role in cancer raise the intriguing possibility
432 that it promotes immune evasion in cancer and may be associated with resistance to
433 immunotherapy. Indeed, NSCLC with high levels of PMSE4 had reduced signature of T cell
434 infiltration and inflammation (Figures 6A, S23). PSME4 and immunoproteasome levels vary
435 greatly among different types of cancer (Figures. 6B and S24A). Therefore, we analyzed RNA-seq
436 data from the CPI1000+ cohort (Litchfield et al., 2021), comprising 6 different patient cohorts of
437 three different cancer types treated with ICI (Van Allen et al., 2015; Hugo et al., 2016; Mariathasan
438 et al., 2018; McDermott et al., 2018; Riaz et al., 2017b; Snyder et al., 2014) and found that PSME4
439 varies greatly among individual tumors and cancer types and that tumors with high expression of
440 PSME4 were less likely to respond to immunotherapy (Figures. 6C-D). This was true within each
441 cancer type examined separately, and when response rate was measured across the CPI1000+
442 cohort (ref) (Figure S24B). Specifically, melanoma, in which the immunoproteasome has been
443 reported to be upregulated and associated with response to therapy(Harel et al., 2019; Riaz et al.,
444 2017a), expressed PSME4 lowly on average whereas renal and bladder cancers exhibited a wide
445 range of expression for both the immunoproteasome and PSME4 (Figure 6C). Since we showed
446 that PSME4 attenuates immunoproteasome activity, we hypothesized that the ratio between
447 PSME4 and the immunoproteasome levels, and not their absolute level, may be a better measure to
448 examine response to ICI. Furthermore, we found that in the PSME4-low cellular state, PSMB10 is
449 the immunoproteasome subunit that is most increased (Figure 3B), so we chose it to categorize
450 immunoproteasome levels in the cohorts. Notably, the ratio of PSME4 to PSMB10 yielded a more
451 significant association to the response to ICI than either subunit alone (Figure 6E, S24B-C). To
452 control for the potential bias of data pooling, we also calculated the effect size across the cohorts
453 by combining the individual effect sizes of each biomarker in each cohort (Figure 6F and S25A-
454 B). PSME4 , PSMB10 and the ratio between them all had strong effect sizes on responsiveness,
455 even in comparison with tumor mutational burden, previously shown to be one of the strongest
456 classifiers of responsiveness to ICI (Litchfield et al., 2021). Furthermore, we showed that PSME4
457 did not strongly correlate with other biomarkers from the cohort and that is still had a significant
458 contribution to a general linear regression model of responsiveness even when the other significant
459 biomarkers, such as TMB were included (Figure S25A; PSME4 - P = 0.0194).

460

461 To demonstrate that the stratification of patients by the ratio of PSME4 and PSMB10 expression
462 translates to NSCLC we validated the signature we observed in the ICI1000+ cohort in a 27 patient
463 NSCLC cohort (Kim et al., 2020). Indeed, we saw that NSCLC patients with low levels of PSME4
464 in the tumor had a higher ICI response rate, consistent with the findings in Melanoma, Bladder and
465 Kidney cancer, albeit not significantly due to the small size. To strengthen this observation, we
466 utilized an Ex-Vivo Organoid Culture model (EVOC(Kamer et al., 2021)), which contain tumor
467 tissue, infiltrating lymphocytes and stroma cells (Figure 6G, S26A-B). We assessed the expression
468 of PSME4 and PSMB10 as well as stained for CD8^+ T cell infiltrates and PDL1 from a section of
469 the resected tumor (Figure S26A-B). In parallel, we tested the IFNγ levels following treatment with
470 either Durvalumab alone (αPD-L1) or together with Ipilimumab (αCTLA-4) in the EVOCs. IFNγ
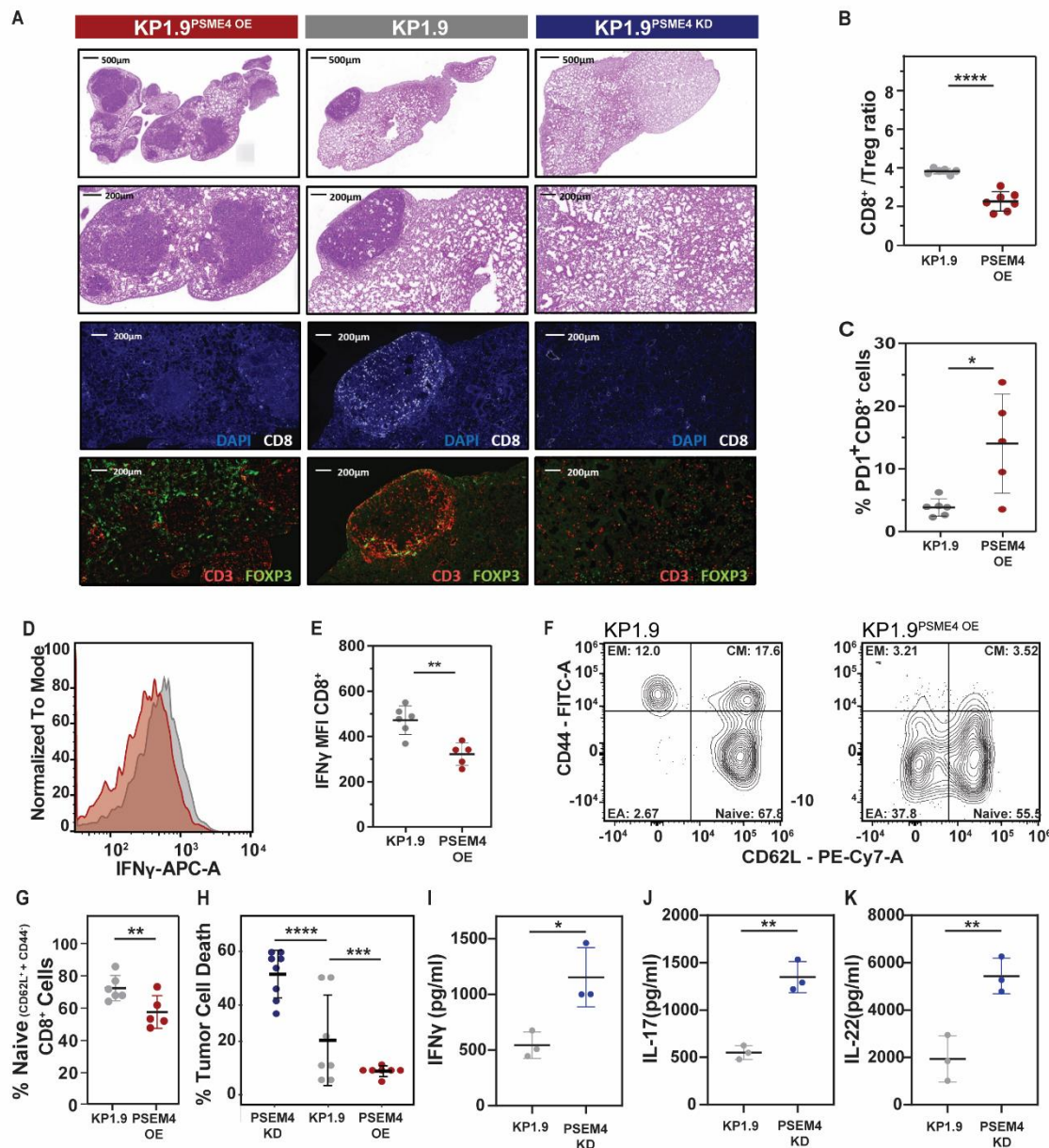
Fig 5. PSME4 abrogates anti-tumor immunity. (A) H&E staining of lungs from mice bearing KP1.9, KP1.9[PSME4 OE], or KP1.9[PSME4 KD] tumors (top) and immunofluorescence staining of the tumor sections with indicated antibodies (bottom). **(B)** The ratio of CD8 T cells to Tregs in the spleens of mice bearing KP1.9[PSME4 OE] or KP1.9 tumors (****P <0.0001). **(C)** The percent of PD1 positive CD8 T cells in the lung of the mice bearing KP1.9[PSME4 OE] or KP1.9 tumors (*P = 0.0440). **(D)** A histogram of IFNγ stained CD8 T cells of mice bearing KP1.9 (grey) or KP1.9[PSME4 OE] (pink) tumors**. (E)** The median fluorescent intensity (MFI) of IFNγ stained CD8 T cells in the lung of mice bearing KP1.9[PSME4 OE] or KP1.9 tumors (E; *P = 0.0017). **(F-G)** The percent of different subsets of CD8-positive lymphocytes (naïve, early activated, effector memory [EM] or central memory [CM], which are CD62L and/or CD44 positive, in the lung of mice bearing KP1.9[PSME4 OE] or KP1.9 tumors. **(H)** The percent of KP1.9 cells co-cultured with splenic lymphocytes from mice bearing KP1.9, KP1.9[PSME4 OE] or KP1.9[PSME4 KD] tumors that is dead (****P <0.0001, ***P = 0.0021). **(I-K)** The amount (pg/ml) of IFNγ (I) , IL-17 (J) or IL-22 (K) secreted from splenic lymphocytes from mice bearing KP1.9 or KP1.9[PSME4 OE] tumors (*P<0.05, **P<0.01).

-14-

485   levels (Kamer et al., 2021) were then used to define a response-like signature in the EVOCs.
486   Notably, we found that tumors with responder hallmarks had significantly lower PSME4/PSMB10
487   ratios compared to non-responders (Figures 6H-I, S26C-F) and that neither PSME4 nor PSMB10
488   individually associated with the response (Figures S26H-I). This result did not merely reflect
489   immune cell infiltration as both PSME4 and PSMB10 were expressed in the epithelial tissue, and
490   PSMB10 was more highly expressed in the lymphocyte infiltrates, consistent with the known
491   expression of the immunoproteasome in immune cells (Figure 6I).

492

493   **Discussion**

494

495   We show that altered proteasome composition and function shape tumor-host interactions in
496   NSCLC and that PSME4-capped proteasome plays an anti-inflammatory role in cancer by
497   attenuating immunoproteasome activity. The attenuated immunoproteasome activity in turn leads
498   to reduced antigenicity by restricting immunopeptidome diversity and altering surface HLA
499   presentation as well as reducing cellular inflammation in an IL-6 dependent manner. While label-
500   free quantitative MS analysis of cell lines suggested that <5% of 20S proteasomes bear PSME4
501   regulators (Fabre et al., 2014; Morozov and Karpov, 2019), our results suggest that this frequency
502   is increased in many cancer types. As PSME4 is associated with DNA damage and histone
503   organization, we speculate that it may be upregulated to offer a protective mechanism to cope with
504   the associated proteotoxic stress and DNA damage (Ahmed, 2019; Kammerl et al., 2019; M. Cantin
505   and V. Richter, 2012; Srinivas et al., 2019). Further, as PSME4 is known to play a nuclear role and
506   was suggested to modulate transcription (Jiang et al., 2021) it will be intriguing to comprehensively
507   examine the effect its upregulation has on the transcriptional landscape, which is beyond the scope
508   of our study. Nevertheless, the dominant effect PSME4 has on the degradation landscape, and the
509   altered catalytic activity of the immunoproteasome even in cell-free systems, strongly suggest that
510   PSME4 exerts its effect also by directly modulating proteasome activity, post-translationally.

511

512   Moreover, we found PSME4 to be the first known example of a regulator differentially modulating
513   the activities of the constitutive proteasome and immunoproteasome. PSME4 is one of a small
514   number of markers of resistance to ICI, as opposed to markers of responsiveness such as the
515   immunoproteasome, TMB, infiltrate signatures and others. As such, it highlights the potential of
516   targeting PSME4 expression or its binding to proteasomes as a novel therapeutic approach in
517   treating NSCLC and in sensitizing response to ICI. Because PSME4 levels are tumor-type specific,
518   such approaches are expected to differ between cancer types. Together, our results highlight the
519   degradation landscape and the balance between different proteasome compositions as an
520   understudied factor in pathogenesis of human diseases in general and cancer proteostasis in
521   particular. This novel proteasome-dependent mechanism of immune evasion allows tumors to
522   abrogate anti-tumor immunity is of particular interest as it provides another layer to the
523   understanding of tumor proteostasis control.

524

525
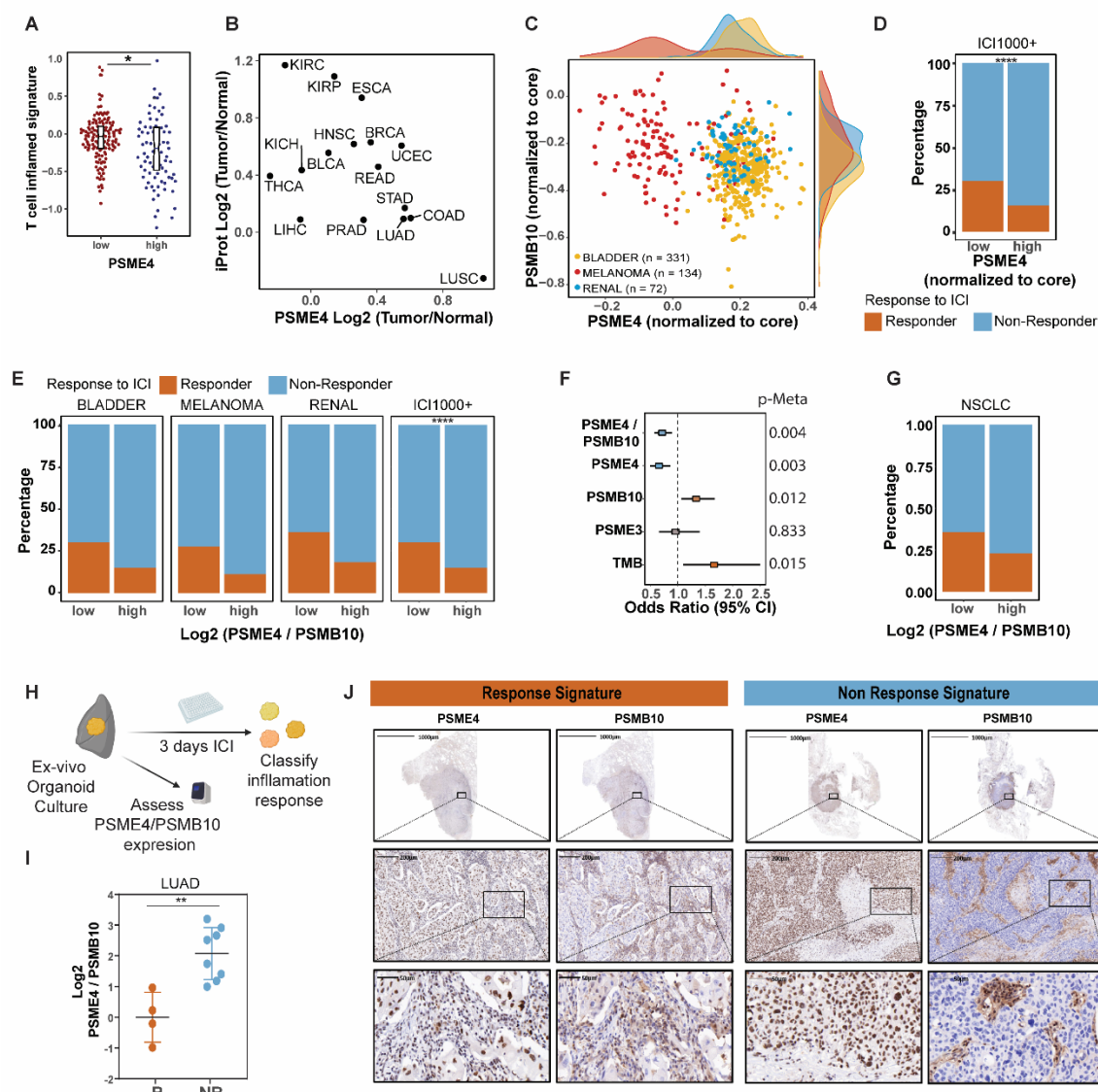
Fig 6 Responsiveness to ICI is reduced in PSME4-high tumors across multiple cancer types. (**A**) T-cell inflammation signature was calculated for the LUAD samples in CPTAC stratified according to the PSME4 expression level. (**B**) The ratio of PSME4 expression in the tumor versus normal tissue from the indicated TCGA cohort is plotted against the ratio of the mean of the immunoproteasome (iProt) subunits PSMB8-10 and PSME1-2 in the tumor versus normal tissue. (**C-E**) The expression of PSME4 normalized to the core proteasome subunits is calculated for bladder cancer, melanoma and renal tumors across the Hugo, Mariathasan, McDermot, Riaz, Snyder, and Van Allen cohorts. PSME4 is plotted against PSMB10 (C). PSME4 normalized to the core proteasome subunits (D) or the ratio of PSME4 and PSMB10 expression (E) was used to stratified patients (upper and lower 50% of samples). The percentage of responders and non-responders to ICI was counted for each group per cancer type and across the CI1000+ cohort (χ2 test D****P = B**** P = 0.000096, E**** P = 0.000016). (**F**) The effect size (calculated as the log2 odds ratio for response versus no response) and significance of the proteasome subunit biomarkers and Tumor Mutational Burden (TMB) in meta-analysis across all cohorts incorporating the effect sizes and standard errors from each individual cohort. The meta p values (p-Meta) are shown on the right. (**G**) The ratio of PSME4 and PSMB10 expression was used to stratified patients who responded to ICI in the NSCLC Kim cohort. (**H**) Workflow of the Ex-Vivo Organoid Culture System (EVOC). A fraction of each resected tumor was assessed for PSME4 and PSMB10 expression using quantitative PCR and the rest was treated for 3 days with immune

544   checkpoint inhibitors (ICI). Response-like signature to ICI was classified by IFNγ expression. **(I)** The ratio

545   of PSME4 to PSMB10 expression determined by qPCR in patient tumors with EVOC ICI responder or non-

546   responder signature (** P = 0.0056). **(J)** Immunohistochemistry for PSME4 and PSMB10 of sections with

547   an ICI response-signature and an ICI non-response-signature EVOC samples.

548   **Materials and Methods**
549
550   **Purification of proteasome complexes.**
551   Lung Adenocarcinoma tumors and adjacent tissues were mechanically disrupted and passed
552   through a 70 µm cell strainer 93070 (SPL). Cells were lysed with 25 mM HEPES, pH 7.4, 10%
553   glycerol, 5 mM MgCl2, 1 mM ATP, and 1:400 protease-inhibitor mixture (Calbiochem), then
554   homogenized through freeze–thaw cycles and passed through a needle. The lysates were cleared
555   by 30-min centrifugation at 21,130g at 4 °C. Lysates were treated with 2 mM 1,10-phenanthroline
556   (Sigma), cross-linked with 0.5 mM DSP (Thermo Fisher Scientific) for 30 min at room temperature,
557   and quenched in 100 mM Tris-HCl, pH 8, 5 mM L-cysteine for 10 min at room temperature. For
558   immunoprecipitation, the lysates were then incubated with Protein G–Sepharose beads (Santa
559   Cruz) with antibodies to PSMA1 and eluted with 100 mM Tris-HCl, pH 8, 8M urea and 50 mM
560   DTT for 30 min at 37 °C. Subsequently, 1% trifluoroacetic acid (TFA) was added. Aliquots of each
561   elution fraction were analyzed by SDS–PAGE to evaluate yield and purity.
562   **Purification and concentration of proteasome peptides.**
563   A critical step in our procedure is the separation of peptides from the proteins eluted in the
564   proteasome pulldown. MAPP analyzes endogenously cleaved peptides, whereas the proteasome
565   complex and associated proteins are physically excluded. Immunoprecipitated proteasomes and
566   their encompassed peptides were loaded on C18 cartridges (Waters) that were prewashed with 80%
567   acetonitrile (ACN) in 0.1% TFA, then washed with 0.1% TFA only. After loading, the cartridges
568   were washed with 0.1% TFA. Peptides were eluted with 30% ACN in 0.1% TFA. Protein fractions
569   were eluted with 80% ACN in 0.1% TFA.
570   **Mass spectrometry sample processing**
571   Protein fraction after proteasome purification; Samples were loaded onto 3 kDa molecular weight
572   cut-off spin columns. Volume was reduced to 25µL by centrifugation at 14,000g for 10min. 175µL
573   8M urea was added and centrifuged at 14,000g for 10min. Filters were reversed and centrifuged to
574   extract the proteins. Proteins were reduced with 5 mM dithiothreitol (Sigma) for 1hr at room
575   temperature and alkylated with 10 mM iodoacetamide (Sigma) in the dark for 45 min at room
576   temperature. Samples were diluted to 2M urea with 50mM ammonium bicarbonate. Proteins were
577   then subjected to digestion with trypsin (Promega; Madison, WI, USA) overnight at 37°C at 50:1
578   protein:trypsin ratio, followed by a second trypsin digestion for 4 hr. The digestions were stopped
579   by addition of trifluroacetic acid (1% final concentration). Following digestion, peptides were
580   desalted using Oasis HLB, µElution format (Waters, Milford, MA, USA). The samples were
581   vacuum dried and stored in -80˚C until further analysis.
582   Total proteomics; Lysates in 5% SDS in 50 mM Tris-HCl were incubated at 96 °C for 5 min,
583   followed by six cycles of 30 s of sonication (Bioruptor Pico, Diagenode, USA). Proteins were
584   reduced with 5 mM dithiothreitol and alkylated with 10 mM iodoacetamide in the dark. Each
585   sample was loaded onto S-Trap microcolumns (Protifi, USA) according to the manufacturer's
586   instructions. In brief, after loading, samples were washed with 90:10% methanol/50 mM
587   ammonium bicarbonate. Samples were then digested with trypsin for 1.5 h at 47 °C. The digested
588   peptides were eluted using 50 mM ammonium bicarbonate; trypsin was added to this fraction and
589   incubated overnight at 37 °C. Two more elutions were made using 0.2% formic acid and 0.2%
590   formic acid in 50% acetonitrile. The three elutions were pooled together and vacuum-centrifuged
591   to dry. Samples were kept at −80 °C until analysis.
592   HLA immunopeptidomics was performed as described previously (Kalaora et al., 2020). In brief,
593   cell-line pellets were collected in triplicate from 2x10E8 cells. Cell pellets were lysed on ice with
594   a lysis buffer containing 0.25% sodium deoxycholate, 0.2 mM iodoacetamide, 1 mM EDTA, 1:200
595   Protease Inhibitor Cocktail (Sigma-Aldrich), 1 mM PMSF and 1% octyl-b-D glucopyranoside in
596   PBS. Samples were then incubated in rotation at 4˚C for 1 hour. The lysates were cleared by
597   centrifugation at 48,000 g for 60 minutes at 4˚C and then passed through a pre-clearing column
598   containing ProteinA Sepharose beads. HLA-I molecules were immunoaffinity purified from

599   cleared lysate with the panHLA-I antibody (W6/32 antibody purified from HB95 hybridoma cells).
600   Affinity columns were washed first with 400 mM NaCl, 20 mM Tris–HCl and then with 20 mM
601   Tris–HCl pH 8.0. The HLA-peptide complexes were then eluted with 1% trifluoracetic acid
602   followed by separation of the peptides from the proteins by binding the eluted fraction to Sep-Pak
603   (Waters). Elution of the peptides was done with 28% acetonitrile in 0.1% trifluoracetic acid. The
604   peptides were dried by vacuum centrifugation.

605   **Liquid chromatography mass spectrometry**
606   Peptide fraction; ULC/MS grade solvents were used for all chromatographic steps. Each sample
607   was loaded using split-less nano-Ultra Performance Liquid Chromatography (10 kpsi nanoAcquity;
608   Waters, Milford, MA, USA). The mobile phase was: A) $H2O + 0.1\%$ formic acid and B) acetonitrile
609   + 0.1% formic acid. Desalting of the samples was performed online using a reversed-phase
610   Symmetry C18 trapping column (180 µm internal diameter, 20 mm length, 5 µm particle size;
611   Waters). The peptides were then separated using a T3 HSS nano-column (75 µm internal diameter,
612   250 mm length, 1.8 µm particle size; Waters) at 0.35 µL/min. Peptides were eluted from the column
613   into the mass spectrometer using the following gradient: 4% to 35%B in 120 min, 35% to 90%B in
614   5 min, maintained at 90% for 5 min and then back to initial conditions.
615   The nanoUPLC was coupled online through a nanoESI emitter (10 μm tip; New Objective;
616   Woburn, MA, USA) to a quadrupole orbitrap mass spectrometer (Q Exactive Plus, Thermo
617   Scientific) using a FlexIon nanospray apparatus (Proxeon).
618   Data was acquired in data dependent acquisition (DDA) mode, using a Top10 method. MS1
619   resolution was set to 70,000 (at 400m/z), mass range of 375-1650m/z, AGC of 3e6 and maximum
620   injection time was set to 100msec. MS2 resolution was set to 17,500, quadrupole isolation 1.7m/z,
621   AGC of 1e5, dynamic exclusion of 40sec and maximum injection time of 150msec.

622   **Mass spectrometry data analysis.**
623   Raw data were analyzed in MaxQuant software (version 1.6.0.16) with the default parameters for
624   the analysis of the proteasomal peptides, except for the following: unspecific enzyme, LFQ
625   minimum ratio count of 1, minimum peptide length for unspecific search of 6, maximum peptide
626   length for unspecific search of 40, and match between runs enabled. A stringent false discovery
627   rate (FDR) of 1% was applied for peptide identification. For the analysis of tryptic digests, the
628   default parameters were set, apart from a minimum peptide length of 6. Masses were searched
629   against the human proteome database from UniprotKB (last update September 2018).

630   **Proteomics processing and label-free quantification.**
631   Peptides resulting from MaxQuant were initially filtered to remove reverse sequences and known
632   MS contaminants. For MAPP peptide fraction we removed antibody and proteasome peptides as
633   contaminants. To decrease ambiguity, we allowed peptides that had at least two valid LFQ
634   intensities out of sample replicates, and we included razor peptides, which belong to a unique
635   MaxQuant 'protein group'. MAPP protein intensities were inferred with MaxQuant. For graphical
636   representation, intensities were log transformed, and in Python v3.6, zero intensity was imputed to
637   a random value chosen from a normal distribution of 0.3 s.d. and downshifted 1.8 s.d. For clinical
638   cohorts, zero intensity was imputed to half the minimum. The presence of missing values reflects
639   both technical and biological variation in the samples. In cases of matched samples ratios were
640   calculated per pair and paired t tests were used. Otherwise, ratios were calculated based on the
641   median of each group and a non-paired student t test was used. The protein fraction of the MAPP
642   analysis was normalized to the mean of the core proteasome subunits (PSMA1-7 and PSMB1-4) to
643   control for efficiency. For comparison of WC proteomics and MAPP data, proteins were ranked by
644   their signed pvlaue: the sign of the fold-change between conditions multiplied by the negative log
645   10 transformed p value. Proteins which had positive (tumor-increased) values were binned into 10
646   groups of equal size. Any proteins which were detected in MAPP but not detected or defined as
647   adjacent -associated in WC proteomics were termed not-detected. The proteins in MAPP or WC
648   proteomics with the top 50 signed p values were presented in heatmaps in Figure 1. For the
649   immunopeptidomics, values from a peptide that was not detected in a treatment pair were not

650 included in the analysis. The binding of peptides was predicted by netMHC based on A549
651 haplotypes as described previously (Javitt et al., 2019b). Any peptide with a binding rank greater
652 than 5 was considered as a contaminant for analysis of the differentially presented peptides.

653 **TCGA and CPTAC analysis.**
654 The cancer genome atlas (TCGA) data was mined using the xenaPython package in Python 3.6.
655 The results shown in this analysis are in whole or part based upon data generated by the TCGA
656 Research Network: http://cancergenome.nih.gov/. The full lung carcinoma cohort (both lung
657 adenocarcinoma [LUAD] and lung squamous cell carcinoma [LUSC] designations, n = 1128, 3A
658 and S10) or the LUAD cohort alone (n = 576,S2) as indicated. For the cross-cancer proteasome
659 ratio the GDC pan cancer dataset was used. PSME4 high tumors in Figure 6 and Figures. S24-25
660 were defined as those with above average expression of PSME4. Only cancer types with 10 or more
661 normal controls were used. Ratios presented are the difference between the means of the normal
662 and tumor groups. Data used in this publication were generated by the Clinical Proteomic Tumor
663 Analysis Consortium (NCI/NIH). The CPTAC LUAD cohort (n = 213) was used. In cases where
664 ratios between the adjacent and tumor samples are presented only those samples with matching
665 controls are used. Otherwise, all the tumor and normal (adjacent control) samples were utilized.
666 The T cell inflammation signature was based on Spranger et al. (Spranger et al., 2015; Trujillo et
667 al., 2018).

668 **Immune checkpoint inhibitor response analysis.**
669 Data reprocessing of six cohorts of ICI treated patients across three cancer types (Van Allen et al.,
670 2015; Hugo et al., 2016; Mariathasan et al., 2018; McDermott et al., 2018; Riaz et al., 2017b;
671 Snyder et al., 2014) was performed as described previously (Litchfield et al., 2021). The expression
672 of different proteasome subunits was examined across the samples. Where noted, proteasome
673 subunit expression was normalized to the core proteasome subunits (PSMA1-7 and PSMB1-4) for
674 each sample. Patients were then stratified by the expression of different subunits (50 percent highest
675 and lowest expressers) and this was correlated with response to ICI which was defined as in
676 (Litchfield et al., 2021). To avoid data pooling a meta-statistics approach was used as described in
677 (Litchfield et al., 2021). Likewise, to confirm the independence of different biomarkers a general
678 linear regression model was used. The model was first generated for 35 biomarkers and then
679 iteratively reduced to only the markers which significantly contributed to the classification. The
680 signatures were confirmed in an independent cohort of NSCLC (Kim et al., 2020).

681 **Statistical analysis and data visualization.**
682 Statistical analyses were performed in R v 3.6.2 and GraphPad Prism v 7.04. In R data was
683 visualized using the complexheatmap (Zuguang Gu et al., 2016) and ggplot (Wickam, 2016)
684 packages. Defaults were used unless otherwise noted. Protein annotation and gene ontology
685 analysis were performed with the gene-set enrichment analysis and protein subcellular localization
686 was extracted from the Human protein atlas (Thul et al., 2017; Uhlen et al., 2017; Uhlén et al.,
687 2015) with "uncertain" or "approved" localization reliabilities excluded.

688 **Antibodies and plasmids**
689 Rabbit anti PSME4 HPA060922 1:1000 WB, 1:300 IF (Sigma), Rabbit anti PSMD11 ab99414
690 1:1000 WB, Mouse anti proteasome 20s PSMA1-7 subunits ab22674 1:1000 WB, Rabbit anti
691 PSMB10/MECL1 ab183506 1:1000 WB, Mouse anti β Actin ab170325 1:5000 WB (Abcam),
692 Rabbit anti PA28alpha/PSME1 9643 1:1000 WB, Rabbit anti PSMB8/LMP7 13635 1:1000 WB
693 and Rabbit anti PA28γ 2412 1:1000 WB (Cell Signaling).

694 human HLA-A,B,C-PE (W6/32, Biolegend 311406), FC, 1:20; mouse CD45.2-PerCP/Cy5.5 (104,
695 eBioscience 45-0454-82), FC, 1:200; mouse CD3e-Super Bright 436 (145-2C11, eBioscience 62-
696 0031-82), FC, 1:100; mouse CD4-APC/Cy7 (GK1.5, Biolegend 100414), FC, 1:200; mouse CD8a-
697 Super Bright 702 (53-6.7, Biolegend 100748), FC, 1:200; mouse CD279 (PD-1)-PE (RPM1-30,
698 eBioscience 12-9981-81), FC, 1:100; mouse IFNg-APC (XMG1.2, eBioscience 17-7311-82), FC,
699 1:160; mouse/human CD44-FITC (IM7, Biolegend 103005), FC, 1:200; mouse CD62L-PE/Cy7
700 (MEL-14, Biolegend 104418), FC, 1:6000; mouse FoxP3-Pe (FJK-16s, eBioscience 12-5773-82),

701 FC, 1:200; mouse H-2Db-FITC (KH95, Biolegend 111505), FC, 1:200; mouse H-2kb-PE (AF6-
702 88.5.5.3, eBioscience 12-5958-82), FC, 1:500; Zombie Aqua (Biolegend 423102), FC, 1:300;
703 Propidium Iodide (Sigma Aldrich P4170), FC, 1 ug/mL; CFSE (Biolegend 423801), FC, 5 uM.
704 Mouse anti alpha-6, produced from hybridoma was a kind gift from Keiji Tanaka. IgG1k isotype
705 antibody (BioLegend, BLG-400139) was used as a control of MAPP method.
706 Goat anti Mouse 488 A11029 1:400, Goat anti mouse 647 A31571 1:400 (Invitrogen), Goat anti
707 Rabbit 647 AB150075 1:400 (Abcam), Goat anti mouse HRP 115-035-205 1:5000, Goat anti
708 Rabbit HRP 111-035-003 1:5000 (Jackson labs).
709 MISSION shRNA targeting mouse or human PSME4 or RFP were obtained from Sigma
710 (TRCN0000176569, TRCN0000178428, TRCN0000158223, TRCN0000157073).
711 pcDNA3.1_PSME4 (Welk et al., 2019) was transfected into A549/KP1.9 cells with Lipofectamine
712 2000 (Thermo Fisher).

713 **Cell culture and drug treatments**
714 A549 were originally obtained from ATCC grown in DMEM and used as model systems for cell
715 biology studies including western blot, biochemistry, and imaging. KP1.9, kindly provided by
716 Alfred Zippelius, were grown in Iscove's MDM. Cells were routinely tested for mycolplasma
717 contamination. Media were supplemented with 10% fetal bovine serum, 1%
718 Penicillin/streptomycin and L-glutamine (2mmol/l) (Biological industries), unless otherwise
719 indicated, at 37 °C with 5% CO2.
720 For TNF-α/IFN-γ activation cells were allowed to seed overnight, and subsequently treated with
721 TNF-α (PeproTech, human; 300-01A or mouse; 315-01A) and IFN-γ (PeproTech, human; 300-02
722 or mouse; 315-05) at 20 ng/ml and 10 ng/ml, respectively, for 24h.
723 Cell death assessment was done by trypan blue staining and counted with Countess II™ automated
724 cell counter (Thermo Fisher) and by Cell titerGlo assay (Promega). Proliferation of mammalian
725 cells were measured by KIT8 assay (Sigma).

726 **Proteasome cleavage reporter assay**
727 Cells were lysed with 25 mM HEPES, pH 7.4, 10% glycerol, 5 mM MgCl2, 1 mM ATP, and 1:400
728 protease-inhibitor mixture (Calbiochem), then homogenized through freeze–thaw cycles and
729 passed through a needle. The lysates were cleared by 30-min centrifugation at 21,130g at 4 °C to
730 remove cell debris. Protein concentration of the supernatant was determined by a NanoDrop
731 spectrophotometer (Thermo Fisher Scientific) by measuring the absorbance at 280 nm.
732 Proteasomal activity in cell fractions was determined by cleavage of the fluorogenic precursor
733 substrate Suc-Leu-Leu-Val-Tyr-AMC (Suc-LLVY-AMC), Ac-Pro-Ala-Leu-AMC (Ac-PAL-
734 AMC), Z-Leu-Leu-Glu-AMC (Z-LLE-AMC), Ac-Arg-Leu-Arg-AMC (Ac-RLR-AMC), Ac-Ala-
735 Asn-Trp-AMC (Ac-ANW-AMC) (Boston Biochem), Z-Leu-Leu-Glu-βNA (Z-LLE- βNA), Ac-
736 Nle-Pro-Nle-Asp-AMC (Ac-nLPnLD-AMC) (Bachem). 10 µM substrate was added to 10 µg total
737 protein/well, and incubated in a reaction buffer (50 mM Hepes, pH 7.5, 1 mM DTT, 5 mM MgCl2
738 and 2 Mm ATP). When using recombinant proteins such as PSME4 [purified as described in(Toste
739 Rêgo and da Fonseca, 2019)] or PSME1 (AB-206168, abcam) 1 nM of each protein was add to 100
740 ul final reaction. Fluorescent increase resulting from degradation of peptide-AMC at 37°C was
741 monitored over time by means of a fluorometer (Synergy H1 Hybrid Multi-Mode Microplate
742 Reader, BioTek) at 340 nm excitation and at 460 nm emission, using the proteasome inhibitor,
743 MG132 (Calbiochem) as background. Resulting product curves were followed for up to 3.5 hours.
744 Each value of fluorescence intensity represents a mean value obtained from three independent
745 experiments.

746 **Immuno-blotting**
747 Cells were lysed in STET buffer (50 mM Tris-HCl, pH 87.5, 150 mM NaCl, 2 Mm EDTA 1%
748 Triton-X and1:400 protease-inhibitor mixture (Calbiochem)). Protein concentration was assessed
749 using BC Assay Protein Quantitation Kit (Interchim). 20 µg of total protein was separated by SDS–
750 PAGE on 4-20% gradient ExpressPlus PAGE M42015 (GenScript) and transferred onto PVDF
751 membranes using iBlot™ 2 Gel Transfer Device (Thermo Fisher Scientific). The membranes were

752 blocked in 5% milk prepared in TBS-0.1% Tween and incubated in primary antibodies overnight
753 at 4°C followed by washing and incubation with secondary antibody. Blots were developed using
754 the ChemiDoc XRS+ Imaging System (Bio-Rad) and band intensities were quantified with imageJ
755 analyzer software.

Immuno-precipitation

757 Cells lysed in 25 mM HEPES, pH 7.4, 10% glycerol, 5 mM MgCl2, 1 mM ATP, and 1:400
758 protease-inhibitor mixture (Calbiochem), then homogenized through freeze–thaw cycles and
759 passed through a needle. The lysates were cleared by 30-min centrifugation at 21,130g at 4 °C to
760 remove cell debris. Pre-cleared cell lysates were prepared by incubating with Protein A/G
761 conjugated agarose beads for 30 min at 4°C with slow rotation. 1 mg Pre-cleared cell lysates were
762 then added to 20 µL of fresh Protein A/G conjugated agarose beads along with 4 µg of antibodies
763 (as described). The mixture was incubated over-night at 4°C with slow rotation followed by three
764 1 ml washes with chilled PBS buffer. The target conjugates were then eluted from beads by mixing
765 protein loading dye (with reducing agents) and heating for 5 min at 95°C followed by denaturing
766 Western blot.

Gel Filtration

768 Gel filtration experiments were performed using Superose® 6 Increase 10/300 GL size exclusion
769 column (GE Healthcare) ÄKTA pure protein purification system (Cytiva). The running buffer used
770 was 25 mM HEPES, pH 7.4, 10% glycerol, 5 mM MgCl2 and 1 mM ATP. The column was
771 calibrated using gel filtration molecular weight standard (Bio-Rad). The following standards were
772 used for calibration: Thyroglobulin (670 kDa, Rs=8.6 nm), γ-globulin (158 kDa, Rs=5.1 nm),
773 Ovalbumin (44 kDa, Rs=2.8 nm), Myoglobin (17 kDa, Rs=1.9 nm), Vitamin B12 (1.35 kDa), and
774 Dextran blue (2 MDa).
775 A 0.1 ml protein sample at a final concentration of 0.4 mg/ml was filtered and chromatographically
776 analyzed using a flow rate of 0.5 ml/min. Absorbance was monitored at 280 nm, elution volumes
777 were determined from UV chromatogram. The partition coefficient, Kav, was calculated from the
778 elution volume of the sample, Ve, and total bed volume, Vt, using the expression: $Kav = (Ve -$
779 $V0)/(Vt - V0)$. Calibration curves and equations were established.

Surface HLA staining in flow cytometry

781 A549 and KP1.9 cells were treated with hTNFα/hIFNγ (as described above) or mTNFα/mIFNγ (as
782 described above), respectively, for 24 hr. Cells were harvested and stained with Live/Dead Aqua
783 staining kit from BioLegend as per manufacturer's protocol. Approximately $1x10^6$ cells were
784 washed, blocked with 2% FCS for 5 min and stained with anti-HLA-A/B/C-PE (A549) or anti-
785 MHCI-Kb-PE/MHCI-Db-FITC (KP1.9) in 100ul for 30 min. Cells were washed and acquired.

Tissues fixation, processing and embedding

787 Tissues were fixed in 4% paraformaldehyde for one week. Dehydration of the tissue was done by
788 serial immersion in increasing concentrations of alcohol (70 to 100%) and removal of the dehydrant
789 with Xylene. The tissue was embedded in paraffin, sectioned at 4 µm and mounted on microscope
790 slides. The slides were placed in an oven for one hour at 60ºC or overnight at 37ºC before
791 immunohistochemically staining.

Immunohistochemistry (IHC) and Immunofluorescence staining

793 H&E stains were performed on an automated device according to manufacturer's instructions. IHC
794 stains were performed on a Benchmark XT staining module (Ventana Medical Systems Inc.; USA)
795 using iVIEW DAB Detection Kit (760-091, Ventana Medical Systems Inc.) or Ultra VIEW
796 Universal DAB Detection Kit (760-500, Ventana Medical Systems Inc.; USA). Antibody details
797 are described above. Following immunostaining, sections were counterstained with hematoxylin
798 (Ventana Medical Systems Inc.), rinsed in distilled water and dehydrated manually in graded
799 ethanols. Finally, the sections were cleared in xylene and mounted with Entellan (Surgipath
800 Medical Industries Inc) on glass slides.
801 The immunofluorescent staining was performed at Molecular Cytology Core Facility of MSKCC
802 using Discovery XT processor (Ventana Medical Systems). Sections were stained with antibodies

803   for CD31 (endothelial cell marker), CD3 (T cells), CD8 (T cells) and FoxP3 (Tregs). Scanning of
804   slides was done by PANNORAMIC SCAN II (3DHISTECH).

IHC staining PSME4

806   Paraffin embedded mouse and human tissues were cut in 3 μm thick sections using the Hyrax M55
807   microtome (Zeiss). Tissue sections were incubated for one hour at 60 °C in order to melt paraffin,
808   deparaffinized by incubating two times in xylene for 5 min and rehydrated in a descending alcohol
809   series (100 %, 90 %, 80 % and 70 % (v/v)) for 1 min. To block endogenous protease activity and
810   to permeabilize sections for nuclear staining they were incubated in a methanol/hydrogen peroxide
811   (80 %/1.8 % (v/v)) solution for 20 min. Tissue sections were rinsed in Milli-Q® water and heat-
812   induced antigen retrieval was performed in citrate buffer pH 6 using a decloaking chamber (Biocare
813   Medical). After washing with TBST unspecific binding sites were blocked for 30 min with Rodent
814   Block M (Biocare Medical). The slides were washed again in TBST and incubated with anti-
815   PSME4 antibody (sc-135512, Santa Cruz) diluted in Antibody Diluent (DAKO) for 1 h at RT. After
816   extensive washing in TBST sections were incubated with MACH 2 Rabbit AP-Polymer (Biocare
817   Medical) for 30 min at RT. Sections were rinsed again in TBST and incubated in Vulcan Fast Red
818   AP substrate solution (Biocare Medical) for 10 min. Tissue sections were washed in TBST and
819   MilliQ® water and hematoxylin counterstaining (Carl Roth) was performed to visualize nuclei.
820   After repeated washing in TBST, sections were dehydrated in ethanol and xylene and mounted
821   using Entellan mounting medium (Merck Millipore). Slides were imaged using the MIRAX
822   scanning system (Zeiss).
823   Stainings were analyzed by an expert clinical pathologist blinded to the sample identity. Tumor
824   staging was done as described previously (Klotz et al., 2019). Semiquantitative scores for PSME4
825   expression were obtained by defining the percentage of PSME4 positively stained tumor areas
826   multiplied by the intensity of staining as graded between 1 (weak) to 3 (strong). Scores were
827   dichotomized into high (>80) and low (<80) expressing tumors with the score 80 representing the
828   median of all samples and PSME4 expression scores were correlated with survival of the patients
829   for this cohort.

q-PCR analysis

831   RNA was extracted using Direct-zol™ RNA MiniPrep R2051 (ZYMO research) mRNA levels
832   were ascertained by RT using High-Capacity cDNA Reverse Transcription Kit (ThermoFisher) real
833   time quantitative PCR using sybr-green (Kapa Biosystems) and the StepOnePlus™ Real-Time PCR
834   Systems (Life Technologies) using the following primers:

Primers for real time PCR

mPSME4	F	GCGTTGGCTGAACAAGTTAATG
mPSME4	R	CTCAGGTCTCATAAGTGCAAGG
hPSME4	F	ATTTGGAGTTACCCTGGAGACC
hPSME4	R	GCAGCTTTTCACGAGTGTTTTG
hPSMB10	F	TCCTTCGAGAACTGCCAAAGA
hPSMB10	R	ATCGTTAGTGGCTCGCGTATC
hTNFa	F	CCACGTCGTAGCAAACCACC
hTNFa	R	TTGAGATCCATGCCGTTGGC
hISG15	F	GAG AGG CAG CGA ACT CAT CT
hISG15	R	CTT CAG CTC TGA CAC CGA CA
hIFIT	F	GATCAGCCATATTTCATTTTGAATC
hIFIT	R	GAAAATTCTCTTCAGCTTTTCTGTG
hIL6	F	TTCTCCACAAGCGCCTTCGGTC
hIL6	R	TCTGTGTGGGGCGGCTACATCT
hA20	F	GCGTTCAGGACACAGACTTG
hA20	R	TTCATCATTCCAGTTCCGAGTATC
hRPS18	F	ATTAAGGGTGTGGGCCGAAG
hRPS18	R	TGGCTAGGACCTGGCTGTAT
hGAPDH	F	CAACGGATTTGGTCGTATTG
hGAPDH	R	GATGACAAGCTTCCCGTTCT
mGAPDH	F	AAGGTCATCCCAGAGCTGAA
mGAPDH	R	CTGCTTCACCACCTTCTTGA

835

836 All values were normalized to the mRNA abundance of housekeeping genes (RPS18 or GAPDH
837 in Human; GAPDH in Mouse). Each primers pair was calibrated using the Absolute Quantification
838 program with increasing concentrations of cDNA.

839 **EVOC preparation**
840 Resected tumors were treated for 3 days, in an Ex Vivo Organ Culture (EVOC) with ICI and
841 responders were classified based on their IFNγ expression as described (Kamer et al.). In short,
842 IFNγ levels were tested following treatment with Durvalumab alone (αPD-L1), or combined with
843 Ipilimumab (αCTLA-4) in the EVOCs. In cases where IFNγ was significantly enriched by at least
844 1.9-fold induction the EVOCs were designated as 'responder', while the rest were termed 'non-
845 responder'. This was recently shown to be a correlate for responsiveness to ICI in patients
846 (Kamer et al.).

847 **Orthotopic lung cancer model**
848 Mouse experiments were conducted according to approved experimental procedures (Approval
849 numbers 04400520-2 and 04990620-1). Male C57Bl/6J mice (Envigo, Israel) or RAG1 -/- (Jackson
850 Laboratory) at the age of 8-10 weeks were injected i.v. with $2x10^5$ cells in 200 µL PBS (Biological
851 Industries, Israel). Mice were observed for adverse effects and weights noted twice a week.
852 Peripheral blood was collected from the tail vein. At the end of experiment, mice were sacrificed
853 by CO_2 asphyxiation and tissues collected to cold PBS.

854 **Tissue processing and flow cytometry staining**
855 Peripheral blood was washed and red blood cells removed by ACK lysis buffer (150 mM NH4Cl,
856 10 mM KHCO3, 0.1 mM EDTA in 0.1x PBS-/-) and washed in flow cytometry buffer (PBS-/-,
857 0.5% BSA, 2mM EDTA).
858 Spleens and lungs were weighted before further processing. The left lung lobe was used for
859 histological analysis of tumor development (hematoxylin and eosin) after fixation in 4%
860 formaldehyde (Biolabs, Israel). Right lung lobes were minced and digested with 5 mL digestion
861 buffer: Collagenase 4 (200U/mL, Worthington Biochemicals), DNase I (100 ug/mL, Sigma
862 Aldrich) in PBS++ supplemented with 2 mM CaCl2 for 20 minutes at 37°C under shaking. Single
863 cell suspensions of spleen and lungs were obtained by straining cells through 100 um strainers and
864 washed in cold flow cytometry buffer. Red blood cells were removed by ACK lysis buffer, washed
865 with flow cytometry buffer and strained again.
866 For intracellular cytokine and transcription factor stainings, cells were incubated for 4 hours with
867 Brefeldin A (Biolegend) and Monensin (Sigma Aldrich). First, viability staining was done with
868 Zombie Aqua (Biolegend) according to the protocols. Cell surface staining was performed in flow
869 cytometry buffer in 100 µL at appropriate dilutions. When needed, cells were fixed and
870 permeabilized with the FoxP3 transcription factor kit from eBioscience (Thermo Fisher Scientific)
871 and stained for FoxP3 and IFNg according to the manufacturers protocol. Samples were acquired
872 on an Attune Nxt with Autosampler and analyzed in FlowJo (V10.7.1, Becton, Dickinson and
873 Company). Exemplary gating strategies are provided Figures S10, S20 and S22)

874 **Cytotoxicity assay**
875 10,000 KP1.9 WT cells were stained with CFSE (5uM; BioLegend), at a cell concentration of
876 1x106/ml), plated onto a 96-well plate and allowed to attach overnight. The following day,
877 splenocytes were isolated from naïve mice, or from mice bearing KP1.9-WT, -PSME4 KD, or -
878 PSME4 OE tumors. Red blood cells were lysed using ACK buffer, cells were washed in PBS, and
879 100,000 splenocytes were plated on top of the tumor cells in RPMI medium + beta-mercaptoethanol
880 (50uM). Co-culture was maintained for 7 days. On day 7, cell supernatants were collected onto a
881 new 96-well plate, and the attached tumor cells were detached with Trypsin containing Propidium
882 Iodide (PI). After cell detachment, the supernatant was used to resuspend the detached cells, and
883 the entire sample was acquired.

884 **Cytokine and chemokine secretion**

885   Tumor microenvironment; 10,000 KP1.9 WT cells were plated onto a 96-well plate and allowed to
886   attach overnight. The following day, splenocytes were isolated from naïve mice, or from mice
887   bearing KP1.9-WT, -PSME4 KD, or -PSME4 OE tumors. Red blood cells were lysed using ACK
888   buffer, cells were washed in PBS, and 100,000 splenocytes were plated on top of the tumor cells in
889   RPMI medium + beta-mercaptoethanol (50uM). Co-culture was maintained for 48h or 7 days. The
890   medium was collected at 48h and 7days by centrifugation. Cytokines and chemokines concentration
891   in the tumor microenvironment were determined by 36-Plex Mouse ProcartaPlex (ThermoFisher,
892   EPX360–26092–901) as per manufacturer's instructions. Samples were acquired on MAGPIX
893   System (Luminex) and analysed by MILLIPLEX Analyst V5.1 Flex.
894   Tumor cells secretion; 10,000 KP1.9 shCtrl or KP1.9 PSME4 KD cells were plated onto a 96-well
895   plate and allowed to attach overnight. The following day cells were treated with mTNFα and mIFNγ
896   mix for 24h in the last 6h ONX-0914 (1µM) (APExBIO, A4011) was added to desired wells. Cells
897   were washed twice and incubated for 24h in fresh medium. The medium was collected flowed be
898   centrifugation. Cytokines and chemokines secretion were determined by 36-Plex Mouse
899   ProcartaPlex (ThermoFisher, EPX360–26092–901) as per manufacturer's instructions. Samples
900   were acquired on MAGPIX System (Luminex) and analysed by MILLIPLEX Analyst V5.1 Flex.
901
902   **Single cells RNA-Seq of CD45+ cells from lung tissues**
903   **CD45+ cell isolation from lung tissues**
904   C57Bl/6J mice were injected with KP1.9 shCtrl or shPSME4 cells (0.25x10^6 cells, i.v.). After 21
905   days, lungs were perfused manually with 3 mL cold PBS w/o Mg/Ca through the right ventricle of
906   the heart and harvested (4x shCtrl, 4x shPSME4) into cold PBS. The lung tissue was cut into pieces
907   and processed using a GentleMACS Octo Dissociator (program 37C_m_LDK_1, Miltenyi Biotec)
908   with the mouse lung dissociation kit (130-095-927, Miltenyi Biotec) according to the
909   manufacturer's protocol. After the run, cells were strained through a 70 um mesh and washed with
910   FACS buffer (0.5% BSA, 2 mM EDTA in PBS without Mg/Ca). Red blood cells were lysed with
911   ACK buffer for 4 minutes, the reaction stopped by addition of cold FACS buffer. Finally, cells
912   were resuspended in FACS buffer with FC block (anti-CD16/CD32, 1:500, Biolegend 101330) and
913   incubated for 5 minutes. Lung cells from shCtrl or shPSME4 were stained with four differently
914   labeled CD45 antibodies (APC, PE/Cy7, FITC, violetFluor 450) for 30 minutes at 4C. Cells were
915   washed with FACS buffer twice, and the shCtrl or shPSME4 samples unified for parallel sorting
916   of the four lung populations. Propidium iodide was added fresh (1 ug/mL) to exclude dead cells,
917   and cells were sorted on BD FACSAria III and BD SORP FACSAria II sorters running on BD
918   FACSDiva software (V8.0.1) using a 85 um nozzle. A gating strategy is provided in the
919   supplementary single cell documentation. Finally, cells were washed twice (PBS w/o Mg/Ca,
920   0.04% BSA) and counted on a Neubauer chamber with trypan blue, and three samples from each
921   condition were chosen (high cell count and viability >90%) for further processing.

Target	clone	color	Company	lot	Cat#	dilution
CD45.2	104	APC	eBioscience	2265360	17-0454-82	300
CD45.2	104	Pe/Cy7	eBioscience	4330432	25-0454-82	300
CD45.2	104	FITC	Biolegend	B250186	109806	300
CD45	30-F11	violetFluor 450	Tonbo	C0451092017753	75-0451	300

922
923   **Single cell RNA-seq using Chromium 10x genomics platform**
924   Single cell RNA-seq libraries were prepared at the Crown Genomics institute of the Nancy and
925   Stephen Grand Israel National Center for Personalized Medicine, Weizmann Institute of Science.
926   Cells were counted and diluted to a final concentration of approximately 1000 cells/□L in PBS
927   supplemented with 0.04% BSA. Cellular suspension was loaded onto Next GEM Chip K targeting

-25-

928 6000 cells and then ran on a Chromium Controller instrument to generate GEM emulsion (10x
929 Genomics). Single-cell gene expression libraries as well as single cell V(D)J libraries were
930 generated according to the manufacturer's protocol using the Chromium Next GEM Single Cell 5'
931 Reagent Kits v2 (Dual Index) workflow. Final libraries were quantified using NEBNext Library
932 Quant Kit for Illumina (NEB) and high sensitivity D1000 TapeStation (Agilent). Libraries were
933 pooled according to targeted cell number, aiming for at least 5,000 reads per cell for V(D)J libraries
934 and 20,000 reads per cell for gene expression libraries. Pooled libraries were sequenced on a
935 NovaSeq 6000 instrument using an SP 200 cycles reagent kit (Illumina).

936 **Raw reads processing**
937 Raw sequencing bcl files were converted to fastq files, aligned to GRCm38 mouse genome, unique
938 molecular identifiers (UMIs) were quantified using Cell Ranger suite (v 6.0.0). V(D)J libraries were
939 mapped to GRCm38 VDJ reference provided by 10x Genomics (v 5.0.0), and clones were
940 identified, counted and summarized with Cell Ranger suite (v 6.0.0). Filtered count matrices were
941 imported into R for further processing.

942 **Clustering and cell type identification**
943 In gene expression libraries low quality cells with more than 10% reads mapping to mitochondrial
944 genome were removed. The Seurat R package (version 4.0.3) was used to normalize and scale
945 expression values for total UMI counts per cell (Stuart et al., 2019). Due to complexity and
946 variability in the immune cell population we performed stepwise clustering (Grün et al., 2015). A
947 detailed clustering strategy is shown in supplementary single cell documentation. First, 2000 highly
948 variable genes were identified using vst method. Dimensionality reduction was done with principal
949 component analysis, with the first 30 principal components used for nearest neighbor graph
950 construction and clustering. For each cluster based on their marker expression we identified
951 whether it belongs to one of the groups: non-immune, B cells, T cells, ILCs, macrophages and DCs,
952 cycling cells and other. Subsequently we performed clustering within each group individually as
953 described above, for each cluster we identified markers (Seurat FindMarkers function) and removed
954 clusters containing doublets, i.e. clusters that did not have any uniquely expressed genes and
955 contained markers specific for of at least 2 abundant clusters. For example, clusters with high
956 expression of Ncr1 (NK cell marker) and Cd79b (B cell marker) was considered doublets.
957 Finally, for each cluster we identified markers (Seurat FindMarkers function) and annotated them
958 through comparison with markers in literature and ImmGen database(Heng et al., 2008; Maier et
959 al., 2020; Rosser and Mauri, 2015)

960 **Functional analysis of cell populations**
961 Gene Ontology analysis was performed using g:Profiler2(Raudvere et al., 2019) with default
962 settings, and multiple hypothesis testing adjustment using all mouse genes as background control.
963 The log10 FDR-adjusted P values were plotted as barplots.

964 **Differential expression analysis**
965 To compare gene expression of each cell type cluster between conditions, we calculated pseudobulk
966 by adding reads from all cells within each cluster in a sample. We then used DESeq2 with default
967 parameters to determine differential expression(Love et al., 2014).

968 **Statistics and reproducibility**
969 All experiments were performed in three individual replicates unless otherwise mentioned. For
970 each experiment, all compared conditions were analyzed by MS at the same time. For the NSCLC
971 study, nine samples from tumors and adjacent tissue were analyzed, one was excluded for poor
972 technical quality. The samples were processed independently and analyzed by MS at the same time
973 to maintain comparability across samples and decrease batch effects.

974 **Ethics Statement**
975 Human lung tissues obtained from patients surgically treated for lung cancer were provided by the
976 Asklepios Biobank for Lung Disease, Gauting, Germany or obtained from the Israel National
977 Biobank for Research. Samples were obtained under the approval of the Ministry of Health IRB
978 approval for the Israel National Biobank for Research, protocol no. 118-2018, or the ethics

979 committee of the Ludwig-Maximilians University Munich according to national and international
980 guidelines (project number 333-10).
981 For the ex-vivo organoid cultures, all patients provided written informed consent for the use of
982 blood samples and tumor specimens for research. This study was approved by the Sheba Medical
983 Center ethics committee.

984 **Code availability**
985 All the code used is available from the corresponding author upon reasonable request.

986 **Acknowledgments**

996 **Author Contributions.**
997 AJ, MDS and YM conceived, designed and interpreted experiments and wrote the manuscript. AL-
998 E and SM provided feedback on the manuscript. MDS, MR, AU, HW-L, AE-L proteomics
999 preparation and SM for in vitro work. MPK and IC in vivo and immunofluorescence. AAK, MPK
1000 and AJ performed and analyzed the scRNAseq experiment. AJ and KL analyzed the ICI cohort.
1001 IK, EBD and OZ conducted the EVOC and immunohistochemistry. VW, ESP, ML, and IK analysis
1002 of German patient cohort. AK managed NSCLC Israeli cohort. MA and MDS immunopeptidomics.
1003 YL Mass spectrometry. ATR and PDF purified recombinant PSME4. MDS performed all other
1004 cellular and biochemical assays. AJ performed all other bioinformatics. JB, YS,EE, NF, CS SM,
1005 and YM funded and supervised the work of respective group members and YM supervised the
1006 study.

1007
1008

1009 **References**
1010 Ahmed, A.M. (2019). The Dual Role of Oxidative Stress in Lung Cancer. In Oxidative Stress in
1011 Lung Diseases, (Springer Singapore), pp. 99–113.
1012 Van Allen, E.M., Miao, D., Schilling, B., Shukla, S.A., Blank, C., Zimmer, L., Sucker, A., Hillen,
1013 U., Foppen, M.H.G., Goldinger, S.M., et al. (2015). Genomic correlates of response to CTLA-4
1014 blockade in metastatic melanoma. Science (80-.). *350*, 207–211.
1015 Antoniou, A.N., Lenart, I., Guiliano, D.B., and Powis, S.J. (2012). Antigen Processing and
1016 Presentation by MHC Class I, II, and Nonclassical Molecules. In Vaccinology: Principles and
1017 Practice, (Department of Infection and Immunity/Centre for Rheumatology, University College
1018 London, London, United Kingdom: Wiley-Blackwell), pp. 29–46.
1019 Arima, K., Kinoshita, A., Mishima, H., Kanazawa, N., Kaneko, T., Mizushima, T., Ichinose, K.,
1020 Nakamura, H., Tsujino, A., Kawakami, A., et al. (2011). Proteasome assembly defect due to a
1021 proteasome subunit beta type 8 (PSMB8) mutation causes the autoinflammatory disorder,
1022 Nakajo-Nishimura syndrome. Proc. Natl. Acad. Sci. U. S. A. *108*, 14914–14919.
1023 Avalle, L., Pensa, S., Regis, G., Novelli, F., and Poli, V. (2012). STAT1 and STAT3 in
1024 tumorigenesis. JAK-STAT *1*, 65–72.
1025 Ayers, M., Lunceford, J., Nebozhyn, M., Murphy, E., Loboda, A., Kaufman, D.R., Albright, A.,
1026 Cheng, J.D., Kang, S.P., Shankaran, V., et al. (2017). IFN-γ-related mRNA profile predicts
1027 clinical response to PD-1 blockade. J. Clin. Invest. *127*, 2930–2940.
1028 Baba, T., and Mukaida, N. (2014). Role of macrophage inflammatory protein (MIP)-1α/CCL3 in
1029 leukemogenesis. Mol. Cell. Oncol. *1*.

1030 Blickwedehl, J., Olejniczak, S., Cummings, R., Sarvaiya, N., Mantilla, A., Chanan-Khan, A.,
1031 Pandita, T.K., Schmidt, M., Thompson, C.B., and Bangia, N. (2012). The proteasome activator
1032 PA200 regulates tumor cell responsiveness to glutamine and resistance to ionizing radiation. Mol.
1033 Cancer Res. *10*, 937–944.
1034 Chong, C., Marino, F., Pak, H., Racle, J., Daniel, R.T., Müller, M., Gfeller, D., Coukos, G., and
1035 Bassani-Sternberg, M. (2018). High-throughput and Sensitive Immunopeptidomics Platform
1036 Reveals Profound Interferonγ-Mediated Remodeling of the Human Leukocyte Antigen (HLA)
1037 Ligandome. Mol. Cell. Proteomics *17*, 533–548.
1038 Collins, G.A., and Goldberg, A.L. (2017). The Logic of the 26S Proteasome. Cell *169*, 792–806.
1039 Coux, O., Zieba, B.A., and Meiners, S. (2020). The proteasome system in health and disease. In
1040 Advances in Experimental Medicine and Biology, (Springer), pp. 55–100.
1041 Driscoll, J., Brown, M.G., Finley, D., and Monaco, J.J. (1993). MHC-linked LMP gene products
1042 specifically alter peptidase activities of the proteasome. Nature *365*, 262–264.
1043 Fabre, B., Lambour, T., Garrigues, L., Ducoux-Petit, M., Amalric, F., Monsarrat, B., Burlet-
1044 Schiltz, O., and Bousquet-Dubouch, M.P. (2014). Label-free quantitative proteomics reveals the
1045 dynamics of proteasome complexes composition and stoichiometry in a wide range of human cell
1046 lines. J. Proteome Res. *13*, 3027–3037.
1047 Fabre, B., Lambour, T., Garrigues, L., Amalric, F., Vigneron, N., Menneteau, T., Stella, A.,
1048 Monsarrat, B., Van den Eynde, B., Burlet-Schiltz, O., et al. (2015). Deciphering preferential
1049 interactions within supramolecular protein complexes: the proteasome case. Mol. Syst. Biol. *11*,
1050 771.
1051 Ferrington, D.A., and Gregerson, D.S. (2012). Immunoproteasomes: structure, function, and
1052 antigen presentation. Prog. Mol. Biol. Transl. Sci. *109*, 75–112.
1053 Gaczynska, M., Rock, K.L., and Goldberg, A.L. (1993). |[gamma]|-Interferon and expression of
1054 MHC genes regulate peptide hydrolysis by proteasomes. , Publ. Online 16 Sept. 1993; |
1055 Doi10.1038/365264a0 *365*, 264.
1056 Gillette, M.A., Satpathy, S., Cao, S., Dhanasekaran, S.M., Vasaikar, S. V., Krug, K., Petralia, F.,
1057 Li, Y., Liang, W.W., Reva, B., et al. (2020). Proteogenomic Characterization Reveals Therapeutic
1058 Vulnerabilities in Lung Adenocarcinoma. Cell *182*, 200-225.e35.
1059 Grün, D., Lyubimova, A., Kester, L., Wiebrands, K., Basak, O., Sasaki, N., Clevers, H., and Van
1060 Oudenaarden, A. (2015). Single-cell messenger RNA sequencing reveals rare intestinal cell types.
1061 Nature *525*, 251–255.
1062 Harel, M., Ortenberg, R., Varanasi, S.K., Mangalhara, K.C., Mardamshina, M., Markovits, E.,
1063 Baruch, E.N., Tripple, V., Arama-Chayoth, M., Greenberg, E., et al. (2019). Proteomics of
1064 Melanoma Response to Immunotherapy Reveals Mitochondrial Dependence. Cell *179*, 236-
1065 250.e18.
1066 Heng, T.S.P., Painter, M.W., Elpek, K., Lukacs-Kornek, V., Mauermann, N., Turley, S.J., Koller,
1067 D., Kim, F.S., Wagers, A.J., Asinovski, N., et al. (2008). The immunological genome project:
1068 Networks of gene expression in immune cells. Nat. Immunol. *9*, 1091–1094.
1069 Hugo, W., Zaretsky, J.M., Sun, L., Song, C., Moreno, B.H., Hu-Lieskovan, S., Berent-Maoz, B.,
1070 Pang, J., Chmielowski, B., Cherry, G., et al. (2016). Genomic and Transcriptomic Features of
1071 Response to Anti-PD-1 Therapy in Metastatic Melanoma. Cell *165*, 35–44.
1072 Javitt, A., and Merbl, Y. (2019). Global views of proteasome-mediated degradation by mass
1073 spectrometry. Expert Rev. Proteomics *16*.
1074 Javitt, A., Barnea, E., Kramer, M.P., Wolf-Levy, H., Levin, Y., Admon, A., and Merbl, Y.
1075 (2019a). Pro-inflammatory cytokines alter the immunopeptidome landscape by modulation of
1076 HLA-B expression. Front. Immunol. *10*.
1077 Javitt, A., Barnea, E., Kramer, M.P.M.P., Wolf-Levy, H., Levin, Y., Admon, A., and Merbl, Y.
1078 (2019b). Pro-inflammatory cytokines alter the immunopeptidome landscape by modulation of
1079 HLA-B expression. Front. Immunol. *10*, 141.
1080 Jiang, T.-X., Ma, S., Han, X., Luo, Z.-Y., Zhu, Q.-Q., Chiba, T., Xie, W., Lin, K., and Qiu, X.-B.

1081 (2021). Proteasome activator PA200 maintains stability of histone marks during transcription and
1082 aging. Theranostics *11*, 1458.
1083 Johnson, D.E., O'Keefe, R.A., and Grandis, J.R. (2018). Targeting the IL-6/JAK/STAT3
1084 signalling axis in cancer. Nat. Rev. Clin. Oncol. *15*, 234–248.
1085 Kalaora, S., Lee, J.S., Barnea, E., Levy, R., Greenberg, P., Alon, M., Yagel, G., Bar Eli, G., Oren,
1086 R., Peri, A., et al. (2020). Immunoproteasome expression is associated with better prognosis and
1087 response to checkpoint therapies in melanoma. Nat. Commun. *11*.
1088 Kamer, I., Bab-Dinitz, E., Zadok, O., Ofek, E., Gottfried, T., Daniel-Meshulam, I., Hout-Siloni,
1089 G., Nun, A. Ben, Barshack, I., Onn, A., et al. Immunotherapy response modeling by ex-vivo
1090 organ culture for lung cancer. Rev.
1091 Kamer, I., Bab-Dinitz, E., Zadok, O., Ofek, E., Gottfried, T., Daniel-Meshulam, I., Hout-Siloni,
1092 G., Ben Nun, A., Barshack, I., Onn, A., et al. (2021). Immunotherapy response modeling by ex-
1093 vivo organ culture for lung cancer. Cancer Immunol. Immunother.
1094 Kammerl, I.E., and Meiners, S. (2016). Proteasome function shapes innate and adaptive immune
1095 responses. Am. J. Physiol. - Lung Cell. Mol. Physiol. *311*.
1096 Kammerl, I.E., Caniard, A., Merl-Pham, J., Ben-Nissan, G., Mayr, C.H., Mossina, A., Geerlof,
1097 A., Eickelberg, O., Hauck, S.M., Sharon, M., et al. (2019). Dissecting the molecular effects of
1098 cigarette smoke on proteasome function. J. Proteomics *193*, 1–9.
1099 Khor, B., Bredemeyer, A.L., Huang, C.-Y., Turnbull, I.R., Evans, R., Maggi, L.B., White, J.M.,
1100 Walker, L.M., Carnes, K., Hess, R.A., et al. (2006). Proteasome activator PA200 is required for
1101 normal spermatogenesis. Mol. Cell. Biol. *26*, 2999–3007.
1102 Kim, J.Y., Choi, J.K., and Jung, H. (2020). Genome-wide methylation patterns predict clinical
1103 benefit of immunotherapy in lung cancer. Clin. Epigenetics 2020 121 *12*, 1–10.
1104 Kimura, A., and Kishimoto, T. (2010). IL-6: Regulator of Treg/Th17 balance. Eur. J. Immunol.
1105 *40*, 1830–1835.
1106 Kitamura, A., Maekawa, Y., Uehara, H., Izumi, K., Kawachi, I., Nishizawa, M., Toyoshima, Y.,
1107 Takahashi, H., Standley, D.M., Tanaka, K., et al. (2011). A mutation in the immunoproteasome
1108 subunit PSMB8 causes autoinflammation and lipodystrophy in humans. J. Clin. Invest. *121*,
1109 4150–4160.
1110 Klotz, L., Y, C., M, L., A, P.-C., A, S., I, K., ME, E., I, L., A, M.-H., KAM, A., et al. (2019).
1111 Comprehensive clinical profiling of the Gauting locoregional lung adenocarcinoma donors.
1112 Cancer Med. *8*, 1486–1499.
1113 Knochelmann, H.M., Dwyer, C.J., Bailey, S.R., Amaya, S.M., Elston, D.M., Mazza-McCrann,
1114 J.M., and Paulos, C.M. (2018). When worlds collide: Th17 and Treg cells in cancer and
1115 autoimmunity. Cell. Mol. Immunol. *15*, 458–469.
1116 Lavin, Y., Kobayashi, S., Leader, A., and Rahman, A. (2017). Innate Immune Landscape in Early
1117 Lung Adenocarcinoma by Paired Single-Cell Analyses In Brief Comparing single tumor cells
1118 with adjacent normal tissue and blood from patients with lung adenocarcinoma charts early
1119 changes in tumor immunity and provides insi. Cell *169*, 750-757.e15.
1120 Li, S., Wu, J., Zhu, S., Liu, Y.J., and Chen, J. (2017). Disease-associated plasmacytoid dendritic
1121 cells. Front. Immunol. *8*, 1268.
1122 Litchfield, K., Reading, J.L., Puttick, C., Thakkar, K., Abbosh, C., Bentham, R., Watkins, T.B.K.,
1123 Rosenthal, R., Biswas, D., Rowan, A., et al. (2021). Meta-analysis of tumor- and T cell-intrinsic
1124 mechanisms of sensitization to checkpoint inhibition. Cell *184*, 596-614.e14.
1125 Liu, Y., Ramot, Y., Torrelo, A., Paller, A.S., Si, N., Babay, S., Kim, P.W., Sheikh, A., Lee,
1126 C.C.R., Chen, Y., et al. (2012). Mutations in proteasome subunit β type 8 cause chronic atypical
1127 neutrophilic dermatosis with lipodystrophy and elevated temperature with evidence of genetic
1128 and phenotypic heterogeneity. Arthritis Rheum. *64*, 895–907.
1129 Livneh, I., Cohen-Kaplan, V., Cohen-Rosenzweig, C., Avni, N., and Ciechanover, A. (2016). The
1130 life cycle of the 26S proteasome: from birth, through regulation and function, and onto its death.
1131 Cell Res. *26*, 869–885.

1132   Love, M.I., Huber, W., and Anders, S. (2014). Moderated estimation of fold change and
1133   dispersion for RNA-seq data with DESeq2. Genome Biol. *15*, 550.

1134   M. Cantin, A., and V. Richter, M. (2012). Cigarette Smoke-Induced Proteostasis Imbalance in
1135   Obstructive Lung Diseases. Curr. Mol. Med. *12*, 836–849.

1136   Maier, B., Leader, A.M., Chen, S.T., Tung, N., Chang, C., LeBerichel, J., Chudnovskiy, A.,
1137   Maskey, S., Walker, L., Finnigan, J.P., et al. (2020). A conserved dendritic-cell regulatory
1138   program limits antitumour immunity. Nature *580*, 257–262.

1139   Mandemaker, I.K., Geijer, M.E., Kik, I., Bezstarosti, K., Rijkers, E., Raams, A., Janssens, R.C.,
1140   Lans, H., Hoeijmakers, J.H., Demmers, J.A., et al. (2018a). DNA damage-induced replication
1141   stress results in PA200-proteasome-mediated degradation of acetylated histones. EMBO Rep. *19*.

1142   Mandemaker, I.K., Geijer, M.E., Kik, I., Bezstarosti, K., Rijkers, E., Raams, A., Janssens, R.C.,
1143   Lans, H., Hoeijmakers, J.H., Demmers, J.A., et al. (2018b). DNA damage-induced replication
1144   stress results in PA200-proteasome-mediated degradation of acetylated histones. EMBO Rep. *19*,
1145   e45566.

1146   Mariathasan, S., Turley, S.J., Nickles, D., Castiglioni, A., Yuen, K., Wang, Y., Kadel, E.E.,
1147   Koeppen, H., Astarita, J.L., Cubas, R., et al. (2018). TGFβ attenuates tumour response to PD-L1
1148   blockade by contributing to exclusion of T cells. Nature *554*, 544–548.

1149   McDermott, D.F., Huseni, M.A., Atkins, M.B., Motzer, R.J., Rini, B.I., Escudier, B., Fong, L.,
1150   Joseph, R.W., Pal, S.K., Reeves, J.A., et al. (2018). Clinical activity and molecular correlates of
1151   response to atezolizumab alone or in combination with bevacizumab versus sunitinib in renal cell
1152   carcinoma. Nat. Med. *24*, 749–757.

1153   Morozov, A. V., and Karpov, V.L. (2019). Proteasomes and several aspects of their heterogeneity
1154   relevant to cancer (Frontiers Media S.A.).

1155   Motosugi, R., and Murata, S. (2019). Dynamic regulation of proteasome expression. Front. Mol.
1156   Biosci. *6*.

1157   Muchamuel, T., Basler, M., Aujay, M.A., Suzuki, E., Kalim, K.W., Lauer, C., Sylvain, C., Ring,
1158   E.R., Shields, J., Jiang, J., et al. (2009). A selective inhibitor of the immunoproteasome subunit
1159   LMP7 blocks cytokine production and attenuates progression of experimental arthritis. Nat. Med.
1160   *15*, 781–787.

1161   O'Donnell, T.J., Rubinsteyn, A., and Laserson, U. (2020). MHCflurry 2.0: Improved Pan-Allele
1162   Prediction of MHC Class I-Presented Peptides by Incorporating Antigen Processing. Cell Syst.
1163   *11*, 42-48.e7.

1164   Qian, M.-X., Pang, Y., Liu, C.H., Haratake, K., Du, B.-Y., Ji, D.-Y., Wang, G.-F., Zhu, Q.-Q.,
1165   Song, W., Yu, Y., et al. (2013). Acetylation-Mediated Proteasomal Degradation of Core Histones
1166   during DNA Repair and Spermatogenesis. Cell *153*, 1012–1024.

1167   Raudvere, U., Kolberg, L., Kuzmin, I., Arak, T., Adler, P., Peterson, H., and Vilo, J. (2019).
1168   G:Profiler: A web server for functional enrichment analysis and conversions of gene lists (2019
1169   update). Nucleic Acids Res. *47*, W191–W198.

1170   Raule, M., Cerruti, F., Benaroudj, N., Migotti, R., Kikuchi, J., Bachi, A., Navon, A., Dittmar, G.,
1171   and Cascio, P. (2014). PA28αβ Reduces Size and Increases Hydrophilicity of 20S
1172   Immunoproteasome Peptide Products. Chem. Biol. *21*, 470–480.

1173   Riaz, N., Havel, J.J., Makarov, V., Desrichard, A., Urba, W.J., Sims, J.S., Hodi, F.S., Martín-
1174   Algarra, S., Mandal, R., Sharfman, W.H., et al. (2017a). Tumor and Microenvironment Evolution
1175   during Immunotherapy with Nivolumab. Cell *171*, 934-949.e15.

1176   Riaz, N., Havel, J.J., Makarov, V., Desrichard, A., Urba, W.J., Sims, J.S., Hodi, F.S., Martín-
1177   Algarra, S., Mandal, R., Sharfman, W.H., et al. (2017b). Tumor and Microenvironment Evolution
1178   during Immunotherapy with Nivolumab. Cell *171*, 934-949.e16.

1179   Rock, K.L., Reits, E., and Neefjes, J. (2016). Present Yourself! By MHC Class I and MHC Class
1180   II Molecules. Trends Immunol. *37*, 724–737.

1181   Rodriguez, A., Perez-Gonzalez, A., and Nieto, A. (2007). Influenza Virus Infection Causes
1182   Specific Degradation of the Largest Subunit of Cellular RNA Polymerase II. J. Virol. *81*, 5315–

1183   5324.
1184   Rosser, E.C., and Mauri, C. (2015). Regulatory B Cells: Origin, Phenotype, and Function.
1185   Immunity *42*, 607–612.
1186   Rousseau, A., and Bertolotti, A. (2018). Regulation of proteasome assembly and activity in health
1187   and disease. Nat. Rev. Mol. Cell Biol. *19*, 697–712.
1188   Salzmann, U., Kral, S., Braun, B., Standera, S., Schmidt, M., Kloetzel, P.-M., and Sijts, A.
1189   (1999). Mutational analysis of subunit iβ2 (MECL-1) demonstrates conservation of cleavage
1190   specificity between yeast and mammalian proteasomes. FEBS Lett. *454*, 11–15.
1191   Schmidt, C., Berger, T., Groettrup, M., and Basler, M. (2018). Immunoproteasome Inhibition
1192   Impaíns T and B Cell Activation by Restraining ERK Signaling and Proteostasis. Front. Immunol.
1193   *9*, 2386.
1194   Snyder, A., Makarov, V., Merghoub, T., Yuan, J., Zaretsky, J.M., Desrichard, A., Walsh, L.A.,
1195   Postow, M.A., Wong, P., Ho, T.S., et al. (2014). Genetic Basis for Clinical Response to CTLA-4
1196   Blockade in Melanoma. N. Engl. J. Med. *371*, 2189–2199.
1197   Spits, M., and Neefjes, J. (2016). Immunoproteasomes and immunotherapy—a smoking gun for
1198   lung cancer? J. Thorac. Dis. *8*, E558–E563.
1199   Spranger, S., Bao, R., and Gajewski, T.F. (2015). Melanoma-intrinsic β-catenin signalling
1200   prevents anti-tumour immunity. Nature *523*, 231–235.
1201   Srinivas, U.S., Tan, B.W.Q., Vellayappan, B.A., and Jeyasekharan, A.D. (2019). ROS and the
1202   DNA damage response in cancer. Redox Biol. *25*, 101084.
1203   Stuart, T., Butler, A., Hoffman, P., Hafemeister, C., Papalexi, E., Mauck, W.M., Hao, Y.,
1204   Stoeckius, M., Smibert, P., and Satija, R. (2019). Comprehensive Integration of Single-Cell Data.
1205   Cell *177*, 1888-1902.e21.
1206   Thul, P.J., Akesson, L., Wiking, M., Mahdessian, D., Geladaki, A., Ait Blal, H., Alm, T.,
1207   Asplund, A., Björk, L., Breckels, L.M., et al. (2017). A subcellular map of the human proteome.
1208   Science (80-.). *356*.
1209   Toste Rêgo, A., and da Fonseca, P.C.A. (2019). Characterization of Fully Recombinant Human
1210   20S and 20S-PA200 Proteasome Complexes. Mol. Cell *76*, 138-147.e5.
1211   Tripathi, S.C., Peters, H.L., Taguchi, A., Katayama, H., Wang, H., Momin, A., Jolly, M.K.,
1212   Celiktas, M., Rodriguez-Canales, J., Liu, H., et al. (2016). Immunoproteasome deficiency is a
1213   feature of non-small cell lung cancer with a mesenchymal phenotype and is associated with a
1214   poor outcome. Proc. Natl. Acad. Sci. U. S. A. *113*, E1555-64.
1215   Trujillo, J.A., Sweis, R.F., Bao, R., and Luke, J.J. (2018). T cell–inflamed versus Non-T cell–
1216   inflamed tumors: a conceptual framework for cancer immunotherapy drug development and
1217   combination therapy selection. Cancer Immunol. Res. *6*, 990–1000.
1218   Uhlen, M., Zhang, C., Lee, S., Sjöstedt, E., Fagerberg, L., Bidkhori, G., Benfeitas, R., Arif, M.,
1219   Liu, Z., Edfors, F., et al. (2017). A pathology atlas of the human cancer transcriptome. Science
1220   (80-.). *357*.
1221   Uhlén, M., Fagerberg, L., Hallström, B.M., Lindskog, C., Oksvold, P., Mardinoglu, A.,
1222   Sivertsson, Å., Kampf, C., Sjöstedt, E., Asplund, A., et al. (2015). Tissue-based map of the
1223   human proteome. Science (80-.). *347*.
1224   Ustrell, V., Hoffman, L., Pratt, G., and Rechsteiner, M. (2002). Pa200, a nuclear proteasome
1225   activator involved in DNA repair. EMBO J. *21*, 3516–3525.
1226   Vizcaíno, J.A., Csordas, A., del-Toro, N., Dianes, J.A., Griss, J., Lavidas, I., Mayer, G., Perez-
1227   Riverol, Y., Reisinger, F., Ternent, T., et al. (2016). 2016 update of the PRIDE database and its
1228   related tools. Nucleic Acids Res. *44*, D447–D456.
1229   Welk, V., Coux, O., Kleene, V., Abeza, C., Trumbach, D., Eickelberg, O., and Meiners, S.
1230   (2016). Inhibition of proteasome activity induces formation of alternative proteasome complexes.
1231   J. Biol. Chem. *291*, 13147–13159.
1232   Welk, V., Meul, T., Lukas, C., Kammerl, I.E., Mulay, S.R., Schamberger, A.C., Semren, N.,
1233   Fernandez, I.E., Anders, H.J., Günther, A., et al. (2019). Proteasome activator PA200 regulates

1234   myofibroblast differentiation. Sci. Rep. *9*, 1–11.
1235   Wickam, H. (2016). ggplot2: Elegant Graphics for Data Analysis (Springer-Verlag New York).
1236   Winter, M.B., La Greca, F., Arastu-Kapur, S., Caiazza, F., Cimermancic, P., Buchholz, T.J.,
1237   Anderl, J.L., Ravalin, M., Bohn, M.F., Sali, A., et al. (2017). Immunoproteasome functions
1238   explained by divergence in cleavage specificity and regulation. Elife *6*, e27364.
1239   Wolf-Levy, H., Javitt, A., Eisenberg-Lerner, A., Kacen, A., Ulman, A., Sheban, D., Dassa, B.,
1240   Fishbain-Yoskovitz, V., Carmona-Rivera, C., Kramer, M.P., et al. (2018). Revealing the cellular
1241   degradome by mass spectrometry analysis of proteasome-cleaved peptides. Nat. Biotechnol. *36*,
1242   1110–1116.
1243   Zuguang Gu, Roland Eils, and Matthias Schlesner (2016). Complex Heatmaps Reveal Patterns
1244   and Correlations in Multidimensional Genomic Data - PubMed. Bioinformatics.
1245